Master's thesis

NTNU
Norwegian University of Science and Technology
Faculty of Natural Sciences
Department of Physics

Camilla Bang

Using atomic force microscopy and second harmonic generation to investigate the effects of ultrasound and microbubbles on the extracellular matrix in 4T1 breast tumors

Master's thesis in Nanotechnology
Supervisor: Catharina de Lange Davies
Co-supervisor: Caroline Einen

June 2022

NTNU
Kunnskap for en bedre verden

Camilla Bang

Using atomic force microscopy and second harmonic generation to investigate the effects of ultrasound and microbubbles on the extracellular matrix in 4T1 breast tumors

Master's thesis in Nanotechnology
Supervisor: Catharina de Lange Davies
Co-supervisor: Caroline Einen
June 2022

Norwegian University of Science and Technology
Faculty of Natural Sciences
Department of Physics

NTNU
Norwegian University of
Science and Technology

ABSTRACT

Combining ultrasound and microbubbles for enhancing drug delivery has shown to increase the penetration length of drugs into the extracellular matrix, but the mechanism behind this is still not entirely clear. In this project, the effect of microbubbles and ultrasound on the extracellular matrix and tumor stiffness of 4T1 breast tumors has been investigated.

The first part of the project involved optimizing the curve fitting of force distance curves, obtained using an atomic force microscope (AFM). These curves were fitted with the Hertz model to obtain the Young's modulus, a measure of stiffness. Four different contact point algorithms were tested: goodness of fit, ΔE, ratio of variances and a combination of the strategies. 2703 force curves were obtained from ten 4T1 breast tumors, five treated and five control. Analysis of these found that the combined strategies gave the best estimated contact point, and this was used in further analysis. Three different fit ranges were also tested: the entire indentation depth, the first 50% of the indentation depth, and the last 50% of the indentation depth. Analysis showed that using the entire indentation depth was the best choice, as it also included all the information of the force curve.

In the second part of the project the Young's moduli between control and treated tumors were compared. The collagen density and organization was also measured, by employing the principle of second harmonic generation (SHG) to image collagen using a multiphoton laser microscope. Entire tilescans of three tumor sections per tumor were obtained. The collagen density was quantified by calculating the collagen area fraction, and the collagen organization by calculating the ratio between the forward and backward propagating SHG signal. These parameters were also compared between control and treated tumors. No statistically significant differences was found between control and treated tumors for the Young's modulus, collagen density or the F/B ratio. The correlation between the Young's modulus and the collagen parameters was also investigated. It found a statistically significant positive trend between the Young's modulus and the collagen density, and a small, not statistically significant, positive trend between Young's modulus and F/B ratio. All parameters showed a tendency to be slightly higher in the tumor periphery than the tumor center.

SAMMENDRAG

For å forbedre leveringen av kreftmedisin til svulster har man sett at bruken av mikrobobler kombinert med ultralyd kan ha en positiv effekt. Denne typen behandling har vist seg å kunne øke distansen legemiddelet beveger seg i svulstens ekstracellulære matrise. Grunnen til dette er likevel ikke helt klar. I denne oppgaven er målet å se på effekten av mikrobobler og ultralyd på den ekstracellulære matrisen i 4T1 brystkreftsvulster.

Første del av oppgaven gikk ut på å optimalisere kurvetilpasning av kraftkurver ervervet ved hjelp av et atomkraftsmikroskop (AFM). Disse kurvene ble tilpasset ved bruk av Hertz model for å finne Young's modulus, et mål på stivhet. Fire forskjellige kontaktpunktsalgoritmer ble brukt, hvorpå én var en kombinasjon av de andre tre. Det var denne kombinerte strategien som ga det beste resultatet når 2703 kraftkurver fra ti 4T1 tumorer ble analysert, fem av tumorene var behandlet og fem var ubehandlet. Denne kontaktpunktsalgoritmen ble så brukt i all senere analyse. Tre forskjellige tilpasningsintervaller ble også undersøkt: én så på hele indenteringsdybden, én på de første 50% av indenteringsdybden og én på de siste 50% av indenteringsdybden. Her viste analysen at det å bruke hele indenteringsdybden var det beste valget for videre analyse, noe som ble styrket av at dette tilpasningsintervallet også fikk med seg all informasjon i kraftkurven.

I den andre delen av prosjektet ble verdiene for Young's modulus sammenlignet mellom ubehandlede og behandlede tumorer. Kollageninnholdet og organiseringen av kollagen ble også undersøkt. Dette ble gjort ved bruk av et multifotonlasermikroskop som tok i bruk det andreharmoniske signalet for å se på kollagen. Her ble det tatt bilder av hele tumorsnitt. Tre tumorsnitt per tumor ble avbildet. Fra disse bildene ble kollagentettheten kvantifisert ved å beregne fraksjonen av arealet i bildet som inneholdt kollagen. Organiseringen av kollagen ble kvantifisert ved å se på forholdet mellom transmittert og reflektert signal gjennom prøven (F/B ratio). Disse parameterne ble også sammenlignet mellom ubehandlede og behandlede tumorer. Ingen statistisk signifikante forskjeller ble funnet mellom de ubehandlede og behandlede tumorene for kollagentetthet, F/B ratio og Young's modulus. Korrelasjon mellom Young's modulus og kollagen ble også sett på, og en positiv statistisk signifikant trend ble funnet mellom Young's modulus og kollagentetthet. En svakere, ikke statistisk signifikant, positiv trend ble også funnet mellom Young's modulus og F/B ratio. Alle de målte parameterne viste også en svak trend til å være høyere i periferien enn i senter av tumorene.

PREFACE

This master thesis is the final project of the study program Master of Science in Nanotechnology, with a specialization in Bionanotechnology, at the Norwegian University of Science and Technology. The project is done as a continuation of a project conducted by the same author in the fall of 2021, there will therefore be some overlap between the two projects. The project was done in association with the Department of Physics.

A big gratitude must be given to my main supervisor Catharina de Lange Davies (Professor, Dept. of Physics), for excellent guidance, on both experimental work and in writing this report. I would also like to thank my cosupervisor Caroline (PhD student, Dept. of Physics) for fruitful discussions regarding experiments, and great feedback on writing the report. She also provided the tumors essential for the experimental work. A special thanks must be given to Astrid Bjørkøy (Senior Engineer, Dept. of Physics), for her great expertise and guidance on the lab equipment, as well as for the necessary lab training. Lastly, I would like to thank all my classmates for five wonderful years.

CONTENTS

1 INTRODUCTION

The tumor microenvironment is complex. It consists of a cellular component including cancer cells, immune cells and fibroblasts. The tumor microenvironment also has its own vasculature, which is characterized by leaky blood vessels and a chaotic blood network. The extracellular matrix provides the tissue with mechanical strength and elasticity, as well as contributing in cell signaling by being a reservoir for growth factors, and giving cells easier access to these factors via integrins. The producers of the extra cellular matrix fibers, the fibroblasts, acquire a constantly activated state in tumors, causing the overproduction of extracellular matrix fibers such as collagen type I and fibronectin. The overproduction of ECM fibers leads to a denser and stiffer ECM [1].

This dense and stiff ECM is a major obstacle for tumor treatment. It acts as a physical barrier on drug delivery, since the drug must penetrate through the ECM to reach the cells. This problem can possibly be overcomed by aiding the drug in transversing the ECM. An example of a treatment exploiting this idea is the combination of ultrasound and microbubbles. The oscillation of the microbubbles in response to ultrasonic waves can assist the drug in transversing the blood vessel wall, and physically push the drug further into the extracellular matrix. It has already been shown that this treatment increases the penetration length of the drug, but the mechanism behind this success is still not entirely clear [2].

As the ECM acts as a barrier against drug delivery, it is of interest to investigate whether the microbubbles and ultrasound treatment might alter this barrier in some way. In this project, the effect of ultrasound and microbubble treatment on the extracellular matrix, and its mechanical properties, in 4T1 breast tumors is investigated. The atomic force microscope is used to obtain force indentation curves, which are curve fitted with Hertz model to obtain the Young's modulus, a measure of stiffness. A multiphoton laser scanning microscope is used to obtained tilescans of collagen, by employing the principle of second harmonic generation. From these tilescans the collagen area fraction and F/B ratio is obtained, which are measures of collagen density and orientation respectively.

This thesis was part of a larger project that also involved looking at nanoparticle accumulation, blood vessel perfusion, collagen and hyaluronic acid. This work was done by Charlotte Årseth, as part of her master's thesis.

2 THEORY

2.1 Tumor biology

2.1.1 The hallmarks of cancer

A tumor [1] can be defined as a mass of uncontrollably growing cells. The transformation from normal cells into malignant tumor cells is a process made up of multiple steps. Hanahan and Weinberg proposed in 2000 the Hallmarks of cancer, suggesting six different physiological changes required for cancer formation and growth; self sufficiency in growth signals, insensitivity to antigrowth signals, evading apoptosis, limitless replicative potential, sustained angiogenesis, and tissue invasion and metastasis. The hallmarks are shown in Figure 1. [3]

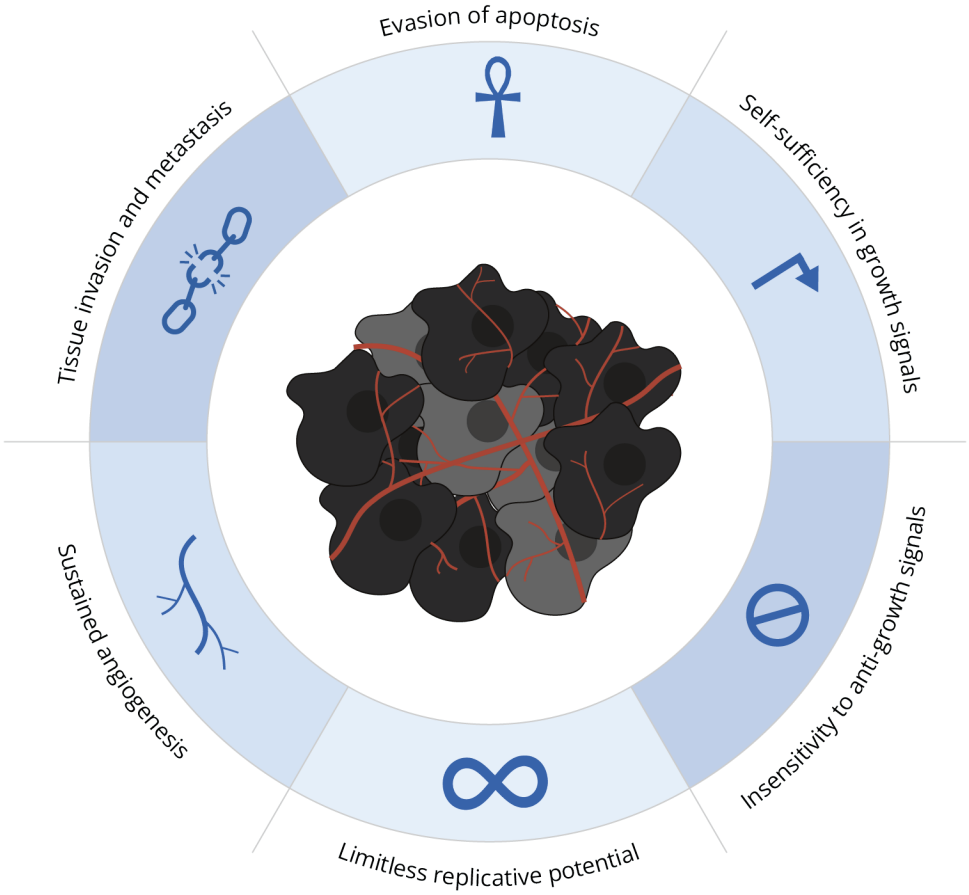

Figure 1: Figure showing the six hallmarks of cancer, which are required physiological changes in cancer cells for the formation and growth of tumors, adapted from Hanahan and Weinberg [3].

1. The word tumor refers to malignant tumors in this thesis and is used interchangeably with the word cancer.

2.1.2 The tumor microenvironment

The previous section described the hallmarks of cancer, necessary properties of cancer cells for tumor development. Tumor tissue is however complex, and consists of more than just cancer cells, as illustrated in Figure 2. The tumor microenvironment (TME) contains the fibers of the extracellular matrix. These fibers provide the tissue with structural strength, and support signal transduction between cells. It also contains blood vessels, supplying oxygen and nutrients to the cellular components of the TME. Lymphatic vessels are present in the tumor periphery, draining excess fluid. The cellular component of the TME include a variety of stromal cells such as immune cells and fibroblasts, in addition to cancer cells [1].

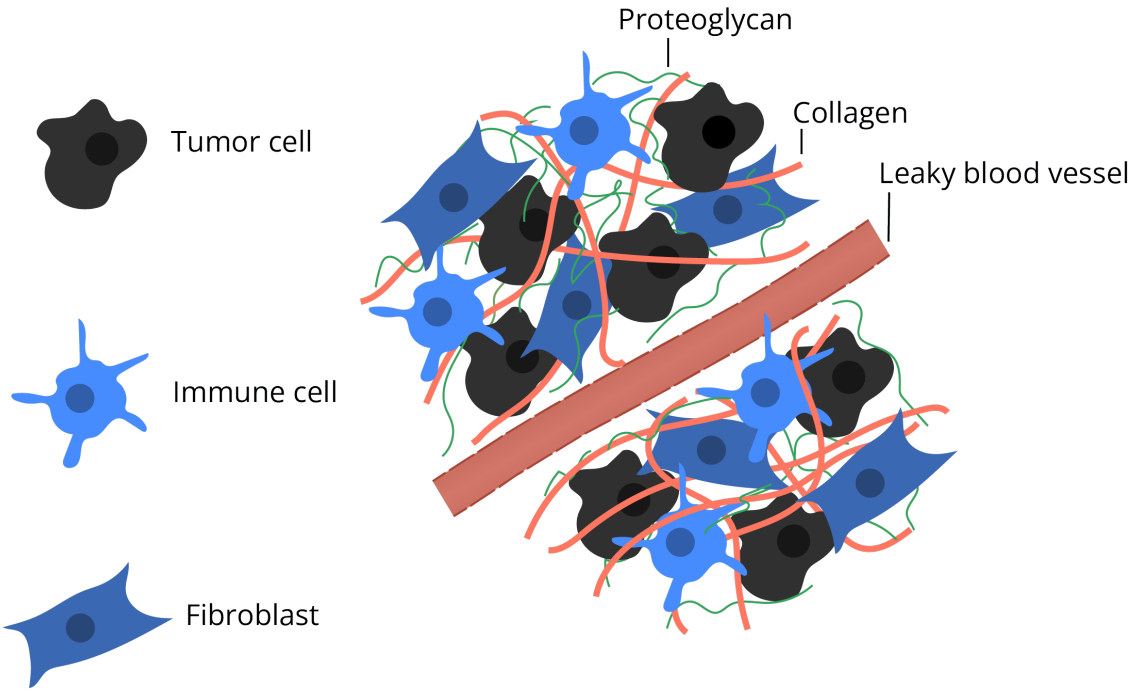

Figure 2: An illustration showing some of the components of the tumor microenvironment; extracellular matrix fibers (collagen and hyaluronic acid), cancer cells, immune cells, fibroblasts and a leaky blood vessel.

All the components of the TME has shown to promote tumor progression in different ways [4]. In this thesis the focus will be on the extracellular matrix; its components, mechanical properties and the effect it has on tumor progression.

2.1.3 The extracellular matrix

The extracellular matrix (ECM) determines the shape and mechanical properties of tissues, and consists of three categories of molecules: structural proteins, proteoglycans and adhesive glycoproteins. The structural proteins, such as collagen, elastin, and fibronectin, provides the ECM with mechanical strength and elasticity. The structural proteins are embedded in a matrix created by the proteoglycans, and the ECM is connected to the cells via the adhesive glycoproteins. Here, we will go further into detail on collagen, and proteoglycans with a focus on hyalorunic acid, a building block of many proteoglycans [5].

Collagen

Collagen provides tissue with tensile strength, and is the most abundant protein in the human body. The structure of collagen is showed in Figure 3, and consists of three polypeptides, termed α chains, forming a triple helix, called the *collagen molecule*. The collagen molecules self-assemble into *collagen fibrils*, which again assemble laterally into a *collagen fiber*. Hydrogen bonds between α chains and collagen fibrills ensures the stability of the collagen fibers. There are about 25 different α chains, forming 15 different types of collagen molecules, with type I being the most abundant [5].

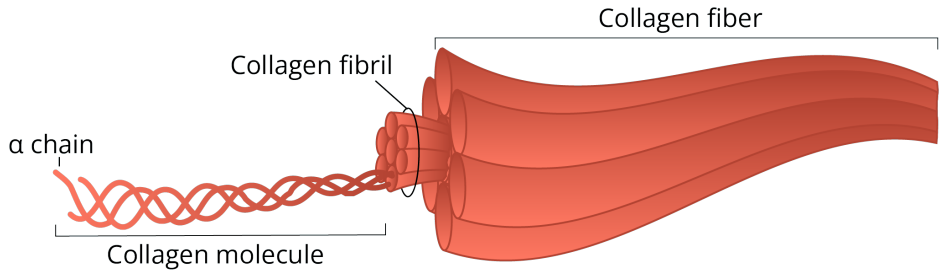

Figure 3: Schematic of the hierarchical structure of collagen. Alpha chains build up a triple helix, forming the collagen molecules, which nest together to form the collagen fibrils, which again forms the collagen fiber.

Proteoglycans

Proteoglycans consists of a protein core, where many glycosaminoglycans are attached, illustrated in Figure 4. Glycosaminoglycans are polysaccharides characterized by a repeating disaccharide unit. One of the most common glycosaminoglycans is hyaluronic acid (HA). Glycosaminoglycans are hydrophilic, and contain negatively charged constituents, attracting both water and cations. This creates a hydrated matrix where the structural proteins are embedded [5].

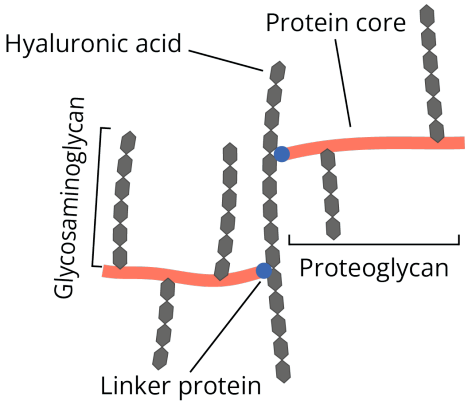

Figure 4: Schematic of the structure of a proteoglycan, which consists of glycosaminoglycans attached to a protein core.

The extracellular matrix and tumor stiffness

Stiffness is a material property, and is defined as the ability of a material to resist deformation when a force is applied. In tissues, the stiffness is mainly determined by the composition and organization of the extracellular matrix [6]. The extracellular matrix fibers can be produced by a variety of stromal cells, but the biggest contributor to ECM production are the fibroblasts [7]. Fibroblasts in healthy tissue are normally quiescent, but in response to tissue damage the fibroblasts will produce ECM fibers. In tumors, the fibroblasts are always in this activated, ECM producing state, and are called cancer associated fibroblasts (CAFs) [8]. These CAFs produce mainly collagen type I and fibronectins. The CAFs can also exert contractile forces on the tissue themselves, via their cytoskeletal elements [9, 10]. The condition of overproduction and accumulation of ECM fibers is called desmoplasia, which is characterized by a continuous ECM production and remodeling. As the tumor stiffness is mainly determined by ECM composition and organization, desmoplasia will also lead to a continuous stiffening of the tumor [6]. Therefore, tumor tissue is often stiffer than healthy tissue [11].

The extracellular matrix in tumors

While the tumor ECM hosts an abundance of both collagen fibers and hyaluronic acid, the constituents are heterogeneously distributed throughout the tumor. When a tumor grows it is restricted by the surrounding healthy tissue. The confined space causes compressive forces to accumulate over time. These compressive forces are largest at the center of the tumor. The gelatinous nature of hyaluronic acid resists compressive forces, and it is therefore mostly deposited in the tumor center. On the other hand, the periphery of the tumor experiences compressive forces in the radial direction, but tensile forces in the circumferential direction. Collagen can provide great tensile strength, and the collagen density at the tumor periphery is therefore ofter higher than throughout the tumor tissue [1, 11].

The role of the extracellular matrix proteins and stiffness in tumor progression

The alterations of the ECM in tumor tissue can increase cancer progression. The extracellular matrix does not only provide mechanical strength, but can also facilitate cell signaling. The ECM provides a reservoir for signaling molecules, and can also assist presentation of these through integrins and proteoglycans. Some of these signaling molecules are growth factors, and the ECM can therefore contribute to sustained malignant cell growth. Some of the growth factors may also be associated with angiogenesis, again sustaining tumor growth [11, 12]. The stiffening can also enhance integrin signaling, which will further encourage tumor growth and progression [13].

It has also been found that cancer cells proliferates at a slower rate in a softer ECM, and the increased matrix stiffness can therefore further increase tumor progression. The stiff ECM can also directly activate signaling pathways involved in cell migration, increasing cell motility, and boosting the invasive potential of the cancer cells [11]. In addition to this, the TME has an increased activity of matrix metalloproteinase (MMP), which contributes to remodeling of the ECM, which in turn can create space for cell migration [13].

The increased matrix stiffness may also inhibit successful vascularization. The ECM fibers can interrupt endothelial cell-cell junctions, leading to leaky blood vessels and reduced blood flow. Furthermore, the increased compressive forces, due to ECM overproduction and rapid tumor growth, can compress both the blood and lymphatic vessels of the tumor. The compression of blood vessels combined with reduced blood flow can lead to hypoxia. Hypoxia in turn can further fuel tumor progression and negatively affect therapeutic efficacy [1, 11].

2.1.4 Drug delivery barriers in tumors

There are three transportation processes required for successful drug delivery: vascular transport into the tumor, the transportation across the blood vessel wall, and the transportation through the interstitial space to reach the cancer cells [1].

A detailed description of the role of the ECM in the tumor microenvironment was given in the previous section, and the stiffening of the ECM is a characteristic of tumor tissue. Another important characteristic is the chaotic blood network. The blood vessels formed through angiogenesis will often have large perforations, causing the vessels to be hyperpermeable and hypoperfused, a characteristic further enhanced by the stiffened ECM, as mentioned above. The hyperpermeable blood vessels causes plasma leakage into the space between the cells of the tissue; the interstitial space. The compressed lymphatic vessels, as a consequence of the increased compressive forces, leads to poor drainage of this excess fluid build up. This leads to a high interstitial fluid pressure (IFP) [1].

The accumulation of plasma due to leaky blood vessels and faulty lymphatic drainage, is termed the enhanced permeability and retention (EPR) effect, and can be beneficial for targeting tumors with therapeutic drugs, as the drug will accumulate in the tumor [14]. The tumor vasculature is however chaotic and poorly organized, and the compressive forces can yield some vessels nonfunctional. Combined with their hypoperfused nature, this can result in a varying distance between blood vessels, and some tumor cells might be harder to reach than others [1].

The transportation across the vessel wall and through the interstitial space is complicated and depends on two different transport mechanisms: convection and diffusion. Convection depends on pressure differences, while diffusion depends on concentration differences. In healthy tissue, the pressure within blood vessels is higher than in the surrounding interstitial space. However, due to the high IFP in tumors, the pressure difference across the vessel wall is very small, rendering the contribution of convection for transvascular transport almost negligible. The uniformly elevated IFP throughout the tumor also means that there are no pressure gradients through the intestritium either, again rendering the transport by convection negligible. The only exception to this is at the tumor periphery, where there is a pressure gradient due to the IFP being higher in the tumor than in the host tissue. This pressure gradient will assist in washing the drugs away from the tumor. At the same time, this pressure gradients means that the IFP will be lower than the pressure within the blood vessels at the tumor periphery. Transport of drugs across the vessel wall and through the interstitium is therefore diffusion dependent in the tumor center, while some transport through convection might happen at the tumor periphery. The transport by diffusion is further limited, because larger drugs are hindered by the dens e ECM [1].

2.2 Ultrasound and microbubbles

2.2.1 Ultrasound principles

Ultrasound is defined as sound waves with frequencies above the human hearing range ($>$ 20kHz) [15]. Sound waves propagate through a medium by the collisions between adjacent molecules in the medium, causing the molecules to oscillate about their origin. Sound waves are normally longitudinal, oscillating in the direction of travel [16, 17]. This is detected as a pressure wave with areas of compression and rarefaction [15], illustrated in Figure 5.

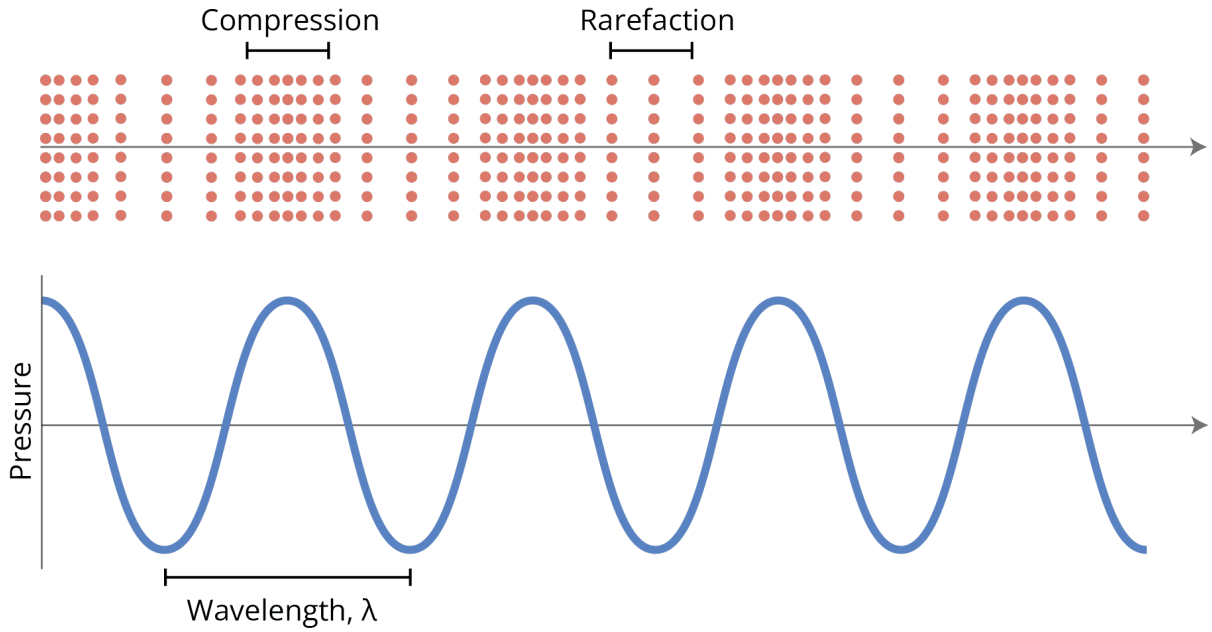

Figure 5: Illustration of an ultrasound pressure wave. The red dots (top) shows the molecules in the path of the wave, which will oscillate, causing areas of compression and refraction. The waves are longitudinal and the wave function (bottom) shows the pressure as a function of distance.

The **wavelength**, λ, is included in Figure 5 and is defined as the distance travelled by the wave in one cycle. The **frequency**, f, is the number of cycles per second. The **velocity**, v, of the sound wave is then defined as the product of the wavelength and the frequency [15–17]:

$$v = \lambda f \tag{1}$$

2.2.2 Generation of ultrasound

A transducer, also called a probe, is used to produce the ultrasonic waves. The transducer contains several piezoelectric crystals, that will expand and retract when subjected to an electric current, ultimately producing pressure waves [16, 18]. Conversely, when the emitted pressure wave is reflected by elements in the medium, and returns to the transducer, the piezoelectric crystals will expand and retract in response to the reflected wave, and an electric current is created [16, 18]. This is the principle for ultrasound imaging.

Acoustic impedance is the term used to describe the resistance that the ultrasonic waves experience when passing through a medium, and it is defined as the product of the wave velocity, v, and the density, ρ of the medium [15]:

$$Z = v\rho \tag{2}$$

Different tissues in the body have different densities, and therefore different acoustic impedances. These differences in acoustic impedance in the path of the ultrasound beam causes the wave to reflect, refract and/or scatter. The reflected wave then returns to the transducer, which translates the wave to a current as explained above, and thus, an image can be formed [16].

The transducer cannot emit and listen for ultrasound waves at the same time. In order to form an image, the transducer therefore must emit ultrasound waves in pulses. The pulses can have different **pulse length**, PL, and **pulse repetition frequency** (PRF), which is the number of pulses emitted per second [18]. The **duty cycle**, DC, is then defined as:

$$DC = PRF \cdot PL \cdot 100\% \tag{3}$$

The duty cycle describes the percentage of time the ultrasound transducer is "on" [19].

Ultrasound-matter interactions

When the ultrasound wave hits a material in its path with different acoustic impedance, some of the wave will reflect. The larger the differences in acoustic impedance, the more the wave will be reflected. If the object is smaller than the wavelength of the ultrasound, the wave will be scattered in all directions. Similarly to light, ultrasound can deviate from its original direction, or refract, when crossing an interface between two materials of different acoustic impedances [16].

As ultrasound travels through tissue, the mechanical energy of the pressure wave will be converted into heat, which is absorbed by the surrounding tissue, ultimately causing the wave to attenuate as it travels. The ultrasound intensity, I, will decrease with traversed distance, x, according to the equation:

$$I = I_0 e^{-ax} \tag{4}$$

where I_0 is the intensity of the transmitted ultrasound. a is the attenuation coefficient and is dependent on ultrasound frequency [20]. Scattering is also a contributing factor to attenuation. A higher frequency wave attenuates faster than one with lower frequency. However, as the frequency is lowered, more of the wave will diffract and scatter, lowering the resolution. Therefore, there is a trade off between penetration depth and resolution [16].

2.2.3 *Ultrasound and microbubbles*

Ultrasound can have therapeutic uses, in addition to being an imaging tool. An important aspect, which will be discussed in this thesis, is the use of ultrasound in combination with microbubbles to enhance drug delivery.

Figure 6 illustrates what happens when a microbubble is subjected to an ultrasound wave. At lower pressure (Figure 6a), the microbubble will oscillate stably, called stable cavitation. While at higher pressures (Figure 6b) the bubble will eventually grow, and subsequently implode. This is called inertial cavitation [19, 21].

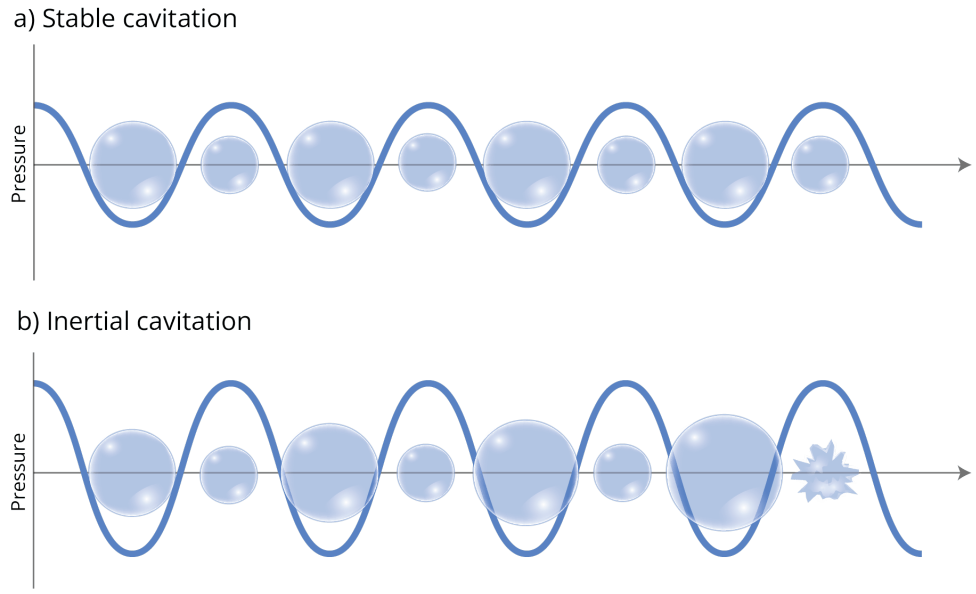

Figure 6: The oscillation of microbubbles in the path of an ultrasonic wave. The ultrasound wave can cause stable cavitation (a), or inertial cavitation (b), which result in the collapse of the microbubble.

Both stable and inertial cavitation can affect drug delivery when the microbubbles are injected to circulate within the blood stream. The different processes are illustrated in Figure 7 During stable cavitation, the blood vessels can expand and retract, causing the gap between endothelial cell junctions to widen in the vessel wall, ultimately enhancing permeability, and facilitating drug extravasation. Another phenomenon of stable cavitation is microstreaming, causing the fluid around the microbubble to move, assisting the drug in penetrating the vasculature. Inertial cavitation can exert great forces as the bubble collapses, resulting in shock waves and liquid jets, creating additional pores in the vasculature. Cavitation can also create pores in the cellular membranes, called sonoporation. The microbubbles can therefore both create pores in the vessel walls for the drug, as well as facilitate drug movement [19].

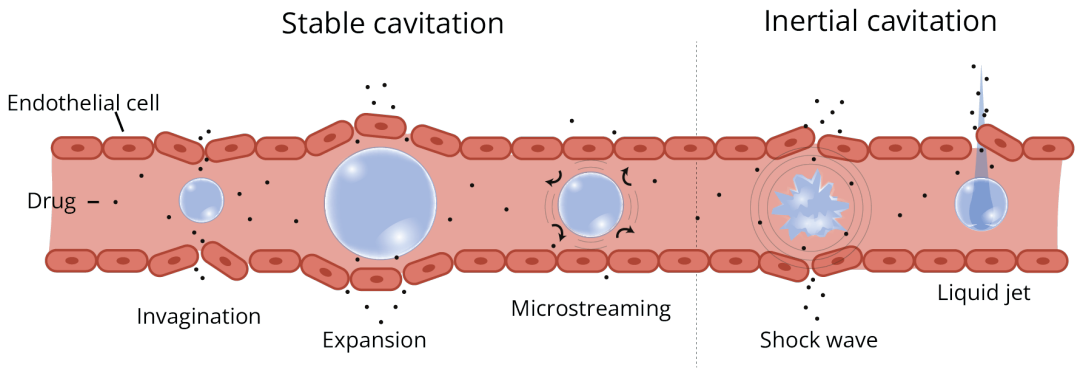

Figure 7: An illustration of the effect of oscillating microbubbles on the blood vessel wall and drug delivery. Adapted from Chowdury et al. [19] and Liu et al. [22].

By focusing the ultrasound on the tumor, the cavitation can be limited to the bubbles present in the vasculature within the tumor, favoring and enhancing drug delivery to the cancer cells.

Ultrasound parameters affecting cavitation

The ultrasound parameters can affect the therapeutic outcome, and it is therefore important to carefully consider. One of these parameters is the frequency, which is very important, as the bubble oscillates with the wave. Frequencies used for therapeutic ultrasound is usually lower than the frequencies used in imaging, and it ranges from a hundred kHz to a few MHz. A lower frequency is often beneficial, as it can penetrate deeper into tissue due to lower attenuation, as explained earlier. Matching the frequency with the resonance frequency of the bubbles can also be beneficial for stable cavitation, as it will increase the amplitude of the oscillation. The oscillation amplitude can be explained as the amount the bubble increases and decreases in volume as it oscillates. The resonance frequency of the bubbles will vary, as it depends on the properties of both the bubbles, such as size and composition, and the surrounding medium [19].

Another important factor to consider, is the ultrasound intensity, as very high intensities can have adverse thermal effects on tissue. These effects can be minimized by delivering the ultrasound in pulses, without notably affecting the drug delivery capabilities. While the intensity is responsible for thermal tissue effects, the **mechanical index** (MI) is a measure of mechanical effects induced on the tissue as a result of cavitation induced tissue damage. The mechanical index is defined as the ratio of peak negative pressure (or peak rarefaction pressure), P_r to the square root of the center frequency, f_c, of the ultrasound beam:

$$MI = \frac{P_r}{\sqrt{f_c}} \tag{5}$$

The mechanical index can therefore be altered by changing the pressure amplitude of the beam, or the frequency. The duration of ultrasound treatment is also important, as treatment effectiveness is related to microbubble oscillation time [19].

2.3 Atomic force microscopy

The invention of the atomic force microscope (AFM) started in 1981 with the invention of the scanning tunneling microscope, a microscope capable of investigating matter on an atomic scale, through tunneling currents in conductive samples. In 1986, the AFM was invented by Bennig, when they saw the need for a microscope capable of conducting the same kind of experiments on non-conductive samples. The invention of the AFM enabled ivestigating atomic scale properties on any flat surface, without the need for any sample preparation [23].

The principle of the AFM is illustrated in Figure 8. A small tip is attached to a cantilever. A laser is reflected off the surface on the top of the cantilever and onto a photodetector. The cantilever is attached to a piezo scanner (not illustrated), which manage to move the cantilever with high precision. In AFM imaging, the tip is a sharp cone, and the cantilever scans the sample. As the tip moves across the sample, changes in the topography causes the cantilever to bend up or down. This deflection causes the laser to move on the photodetector, which measures the deflection in terms of voltage differences, and the topography of the sample can therefore be detected and recorded, creating a topographic image as the tip scans the surface of the sample. A feedback loop connected to the z-piezo scanner will then adjust the height to ensure a constant deflection (contact mode), or a constant tip - sample interaction force (dynamic mode) [23, 24].

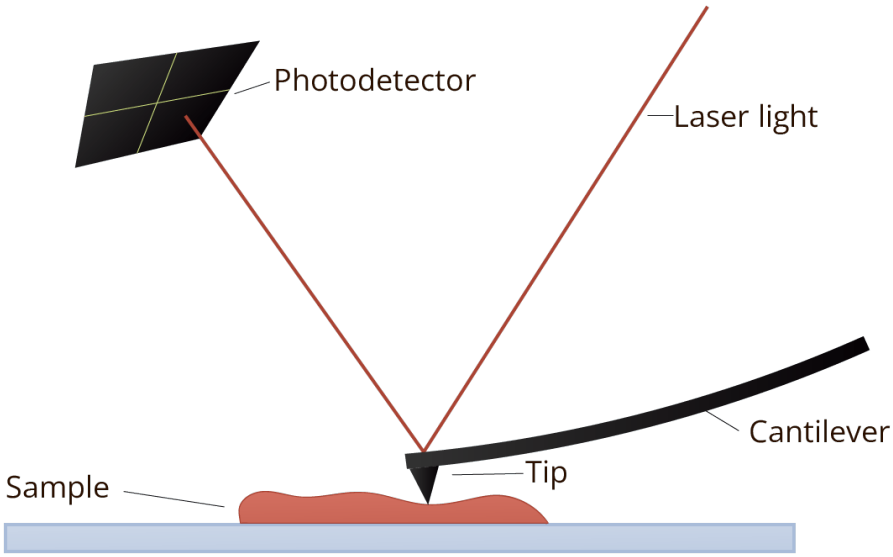

Figure 8: The principle of an AFM. A cantilever with a tip scans the surface of the sample. The laser light reflects off the surface of the cantilever and onto a photodetector. The position of the laser spot on the photodetector will move as the cantilever deflects due to changes in the sample height.

Since its invention, the use of the AFM has only grown larger and tips and cantilevers in many different shapes and sizes have been invented. One of the major advantages of the AFM, is that it also works in a liquid environment, making it a useful tool in investigating biological samples [24].

2.3.1 Force spectroscopy

While imaging surface topography was among the first uses of the AFM, it has evolved into a powerful tool for also looking at mechanical properties. This is done through the acquisition of force distance curves, often only termed force curves. The principle is illustrated in Figure 29a. The force curve acquisition starts above the surface of the sample. The tip approaches the sample at a given speed. As it gets close to the sample, attractive Van der Waahls forces between the tip and the sample will occur, causing the tip to snap into contact, and the cantilever to bend downwards, resulting in a negative voltage measured by the photodetector. As the cantilever moves further down, it will eventually start to push into the sample, causing the cantilever to bend the other way, and a positive voltage is recorded. The tip will keep pushing into the surface, and the cantilever will keep bending, until a given threshold value for the deflection is reached. The probe is then retracted from the surface, and the cantilever relaxes until it again bends the other way, due to the attractive Van der Waahls forces causing the tip to stick to the surface [24]. Figure 29a shows an example of a force curve obtained in air. Figure 29c shows the equivalent curve obtained in a liquid environment. As can be seen in the figure, the characteristic dip in the force curve due to Van der Waahls forces is not present. This is due to Van der Waahls forces being very small and easily disturbed [25].

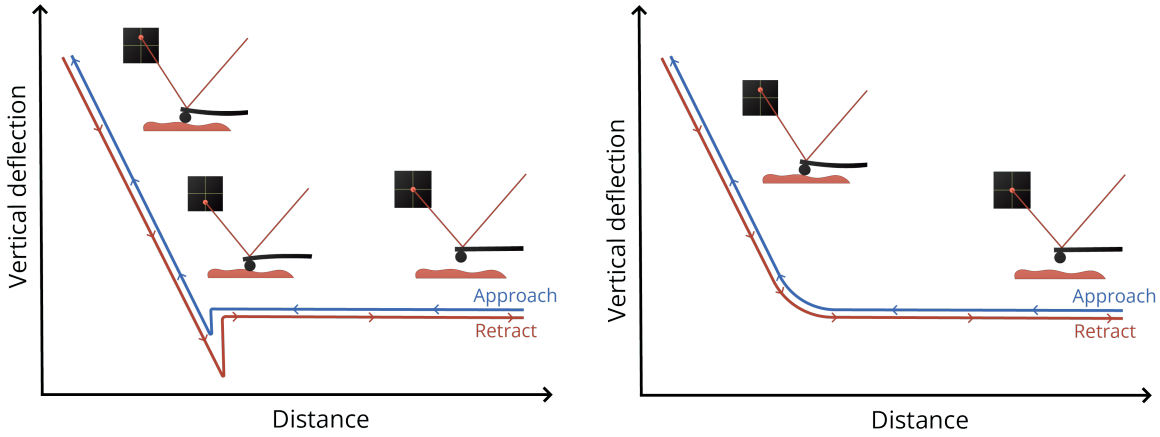

Figure 9: Figures exemplifying force distance curves obtained in air (a) and liquid (b). Illustrations of the cantilever, and resulting laser position, as it approaches the sample are also included. In (a) the tip will snap into contact with the sample as it gets close, due to Van der Waahls forces, causing a dip in the curve. Subsequently, the tip will bend the opposite way as it experience resistance from the sample, and the vertical deflection will increase. In (b) the same steps are included, except the second phase where the tip snaps into contact due to Van der Waahls forces, as Van der Waahls forces are small and easily disturbed.

The acquisition of a force curve, where the tip approaches and retracts from the surface, is termed a ramp, and this mode of operation is often called ramping mode.

To measure mechanical properties it is necessary to translate the measured voltage into force, F. This is done through Hookes law [24]:

$$F = k\Delta d \tag{6}$$

where k is the spring contant of the cantilever, found by acquiring a thermal noise spectrum, and determining the resonance frequency of the cantilever [26]. Δd is the deflection, which can be found from the measured change in voltage, ΔV, via:

$$\Delta d = S \cdot \Delta V \tag{7}$$

where S is the deflection sensitivity of the cantilever, given in nm/V, and obtained through calibration by ramping on a stiff substrate prior to the measurements. The distance shown in Figure 9 is the distance traveled by the z-piezo. The depth the tip travels into the substrate, called the indentation depth, is often more interesting and can be found through the equation:

$$\delta = Z - Z_0 - \Delta d \tag{8}$$

where Z is the total distance travelled by the z-piezo, and Z_0 is the distance traveled by the z-piezo at the contact point between the tip and the sample.

2.3.2 Hertz model

The Young's modulus, or the elastic modulus, is often used as a measure of stiffness. It is an intrinsic material property and is therefore independent on shape and size. The Young's modulus is defined as the ratio between stress (σ) and strain (ε), when an object is subjected to two equal, but opposite, uniaxial forces. The concepts of stress and strain are shown in Figure 10. The stress is defined as the ratio between the force and the crossectional area. The strain is defined as the ratio between the change in length and the original length along the axial direction. A stiffer material will result in a higher Young's modulus, as the strain will be smaller with the same applied force [27–29].

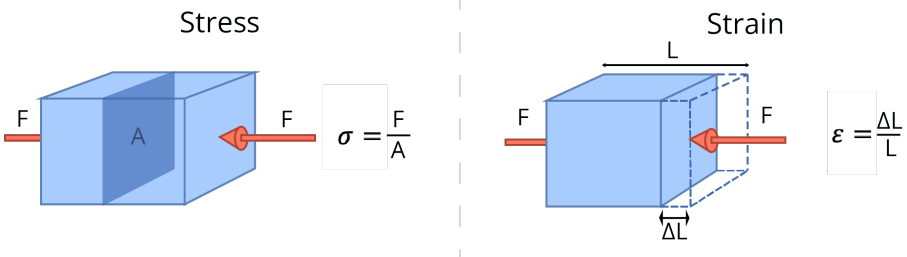

Figure 10: Illustration showing the concepts, and equations, of stress (σ) and strain (ε) as an object is subjected to two equal, but opposite, uniaxial forces, F.

The Young's modulus can be extracted from force curves by using Hertz model. Hertz model, illustrated in Figure 11, assumes a spherical indenter, pushing into a surface with force F, resulting in an indentation depth δ. The Young's modulus, E, is related to the force and indentation depth via the equation[30, 31]:

$$F = \frac{4}{3}\frac{E}{(1-\nu^2)}R^{1/2}\delta^{3/2} \tag{9}$$

where R is the radius of the indenter. ν is the Poisson ratio and is illustrated in Figure 12. It is defined as the ratio between the strain in axial and lateral direction when the material is subjected to two equal but opposite uniaxial forces [32]. For biological tissues, the Poisson ratio is estimated to be around 0.5, and is termed an incrompessible material, meaning that the volume stays constant under an applied force [33].

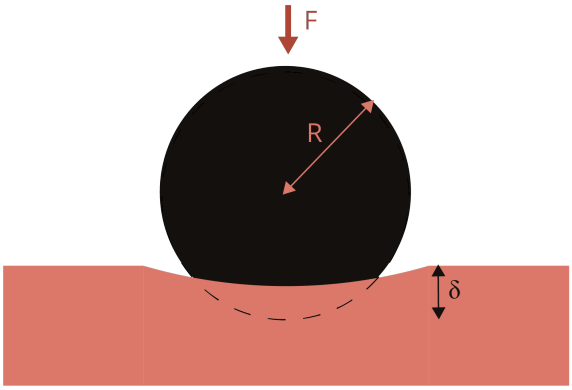

Figure 11: Figure showing the experimental basis for using the Hertz model, where a spherical indenter with radius R pushes into a sample with a force F, resulting in an indentation depth δ. These three parameters can be used to calculate the Young's modulus.

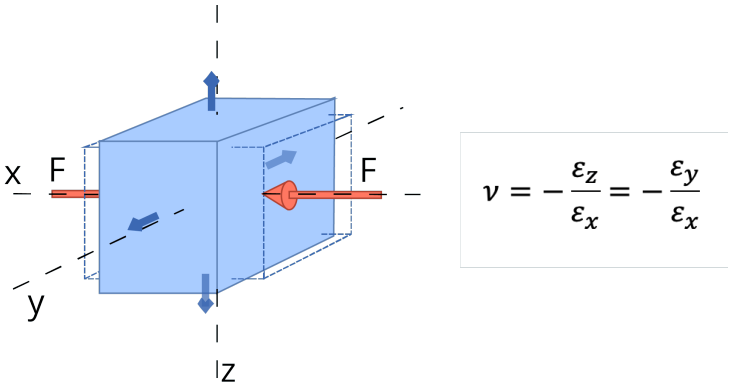

Figure 12: Illustration showing the concept and equation for the Poisson ratio as an object is subjected to two equal, but opposite, uniaxial forces, F. The strain in the lateral directions, y and z, are equal.

Limitations

The Hertz model assumes that the sample is an elastic half space. This means that the sample is homogeneous and isotropic, and extends infinitely in all directions, with the top surface as a boundary. A biological sample can therefore not be considered an elastic half space. However, given a small enough indentation depth, and a small tip radius relative to the sample, a biological sample can be approximated as one. Buckle's rule state that the indentation depth should not exceed 5-10% of the sample thickness, to avoid the stiffness of the underlying substrate to affect the measurements. The distance from the tip to the edge of the sample should be larger than ten times the tip radius, approximating an infinite horizontal extension [34].

Another criterion of the Hertz model not met by biological samples, is that the sample is elastic. An elastic sample will return to its original shape as soon as the load is released. However, biological samples are viscoelastic, meaning that the return to its original form is time dependent. This is often evident in the form of hysteresis between the retract and approach curves [35].

Even though biological samples fail to meet the many criteria of the Hertz model, it has been shown that by careful experimental control, such as attentive choices on indentation depth and probe size, the Hertz model has shown to be a good fit to experimental data. This, combined with the simplicity of the model, is probably why it is one of the most used models in indentation experiments [36].

2.3.3 Determining the contact point of force curves

The Hertz model is based on the indentation depth and not the z-piezo distance. The indentation depth can be found from the z-piezo data, using Equation 8. However, this equation requires that the location of the contact point, Z_0, is known. For force curves obtained in air, the contact point is easily located as a sharp change in the curve, seen as the "dip" in Figure 29a. However, in liquid, the transition from non-contact to contact is often more diffuse, as seen in Figure 29c. Núria Gavara (2016) investigated multiple algorithms for determining the contact point on AFM force curves obtained from living cells [37]. Some of these algorithms will be highlighted and tested in this thesis. The test involves using all points on a force curve as trial points. At each trial point a calculation will be made, according to the chosen algorithm, and the trial point yielding the best value according to a set criterion will be chosen as the contact point.

Goodness of fit

For the goodness of fit method a constant interval is chosen from the trial point, the trial point is then chosen as Z_0 and the Hertz model is fit to this interval. Then the r^2 is calculated for that fit. The trial point at which the highest r^2 is calculated is determined as the contact point. [37]

Change in Young's modulus (ΔE)

The principle of the ΔE method is that the calculated Young's modulus changes more around the contact point than anywhere else on the force curve. Just as for the goodness of fit method, a constant interval is chosen from the trial point, which is set as Z_0 and the Hertz model is fit to this interval. ΔE is then defined as [37]:

$$\Delta E = -\frac{d(lnE)}{di} \tag{10}$$

where i is the trial point and E(i) is the Young's modulus calculated from trial point i. From this, the contact point is determined as the trial point yielding the highest value for ΔE. [37]

Ratio of variances

The ratio of variances method is based on the deflection signal and not the Young's modulus. It assumes that the variance of the deflection signal is larger in an interval around the contact point, than in the non-contact region or the contact region. That means that looking at two intervals, of size N, on both sides of the trial point, the variances of these intervals will be similar if the trial point is well within the non-contact or contact region. The ratio of variances in trial point, i, can be written as [37]:

$$RoV_i = \frac{var(d_{i+1} : d_{i+N})}{var(d_{i-N} : d_{i-1})} \tag{11}$$

where d_i is the deflection signal at trial point i. The contact point is then identified as the point where RoV is the largest. [37]

Combined strategies

In his paper, Gavara also looks at combining multiple strategies for determining the contact point. This is done by multiplying the data from the three aforementioned method and choosing the trial point that has the highest value of $r^2 \cdot \Delta E \cdot RoV$ [37].

2.4 Second Harmonic Generation

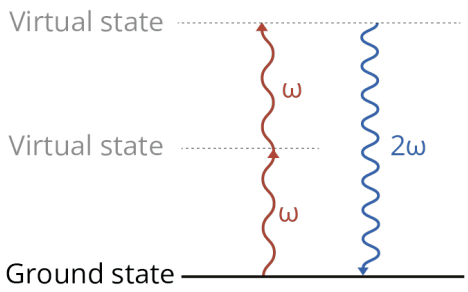

Figure 13: Illustration showing the principle of second harmonic generation, where a photon with frequency ω interacts with matter, resulting in the emission of a photon with twice the frequency, 2ω .

Second harmonic generation (SHG) is a physical phenomenon where two photons with a given frequency interact with matter to form and emit a new photon with twice the incoming frequency, without energy loss. The principle is illustrated in Figure 13.

The polarization P of a medium subjected to an electric field E can be expressed as [38]:

$$P = \epsilon_0\chi^{(1)}E + \epsilon_0\chi^{(2)}E^2 + \epsilon_0\chi^{(3)}E^3 + ... \tag{12}$$

where ϵ_0 is the electric constant. $\chi^{(i)}$ is the susceptibility tensors, dimensionless material properties indicating the degree of polarization of the material in response to the electric field. $\chi^{(1)}$ is a linear susceptibility tensor and is dimensionless, while $\chi^{(i>1)}$ are termed non-linear susceptibility tensors and have units of $(m/V)^{n-1}$. At low electric fields the $E^{n>1}$-terms can be approximated to 0, and the polarization is said to be linear [38].

At high laser intensities (high electric fields), or in media with high hyperpolarizability (high $\chi^{(2)}$) , the polarization depends non-linearly on the electric fields and is given by the equation above. When discussing second harmonic generation, the $\chi^{(2)}$ term becomes important, and the polarization equation is often simplified to only include the first two terms [38]:

$$P = \epsilon_0\chi^{(1)}E + \epsilon_0\chi^{(2)}E^2 \tag{13}$$

The electric field can be expressed as:

$$E = E_0 cos(\omega t) \tag{14}$$

Inserting this into equation (13) gives:

$$P = \epsilon_0\chi^{(1)}E_0 cos(\omega t) + \epsilon_0\chi^{(2)}E_0^2 cos^2(\omega t) \tag{15}$$

Which can be expanded using trigonometric identities to:

$$P = \epsilon_0\chi^{(1)}E_0 cos(\omega t) + \frac{1}{2}\epsilon_0\chi^{(2)}E_0^2 + \frac{1}{2}\epsilon_0\chi^{(2)}E_0^2 cos(2\omega t) \tag{16}$$

The first term describes a polarization vibrating with frequency ω and the third term describes a polarization vibrating with frequency 2ω, producing electromagnetic waves with these frequencies [38].

2.4.1 Imaging collagen using second harmonic generation

Second harmonic generation poses restrictions on the structures that can be imaged. First of all, they must be noncentrosymmetric in the order of λ_{SHG}, in order to produce a visible signal. Secondly, the material must have permanent dipoles, as the polarization equations discussed in the previous section applies to dipoles. Finally, the structures must be ordered so that the second susceptibility tensor, $\chi^{(2)}$ is non-zero. There are three main proteins that fulfill these criteria: fibrillar collagen type I and II, and myosin [39].

To image collagen using second harmonic generation one can use a multiphoton laser scanning microscope equipped with a high intensity laser. The SHG signal generation is intrinsically optically sectioned, meaning that the signal arises only from the scanned focal plane, so a pinhole is not needed [39].

The emitted photons obtained through SHG all have the same frequency and wavelength, and are in phase, meaning that the light is coherent. This results in different emission patterns in the forward and backward direction, in respect to the laser propagation. If the phase of the incoming and the SHG photons are in perfect phase match, the signal will be exclusively forward directed and co-propagating with the laser. Due to the randomness of the distribution of collagen fibers in biological tissue, the phase matching between incoming and SHG photons will be imperfect. This leads to a distribution of forward and backwards emitting photons due to scatterers on the size of λ_{SHG} in the light path. In general, the less regular the arrangement of the collagen fibers is, the higher the backward signal, resulting in a lower forward to backward ratio (F/B ratio) [39, 40].

2.5 Inter- versus intraheterogeneity

If a sample size can be divided into subgroups of samples, it can be of value to evaluate how much of the contribution of the heterogeneity in the sample population comes from heterogeneity within the subgroup (intraheterogeneity, σ^2_{intra}) compared to the heterogeneity between the subgroups (interheterogeneity, σ^2_{inter}). The inter-heterogeneity is defined as the variance of the measured values of all samples. While the intraheterogeneity can be defined as:

$$\sigma^2_{intra} = \frac{\sum_{i=1}^{r}\sum_{j=1}^{n_i}(X_{ij} - \bar{X}_i)^2}{N - r} \tag{17}$$

Where r is the number of subgroups, n_i the number of samples measured in subgroup i, N is the total number of samples, X_{ij} is the measured value of sample j in subgroup i and $\bar{X}_i$ is the average measured value of supgroup i[41].

The relative contribution of intraheterogeneity to the total heterogeneity can then be given as:

$$f = \frac{\sigma^2_{intra}}{\sigma^2_{intra} + \sigma^2_{inter}} \tag{18}$$

where f spans from 0 to 1, where a value of 0.5 means an equal contribution of inter- and intra-heterogeneity. A value above 0.5 means that the contribution to the heterogeneity is larger from within the subgroups, than between the subgroups [41].

3 MATERIALS AND METHODS

3.1 Tumor preparation

3.1.1 Inoculation

A 4T1 murine breast cancer cell line was used for the experiments. 10000 4T1 cells in 50 µL cell medium was injected subcutaneously into the hind leg of ten mice[2]. Five mice were used for control and five mice were treated with ultrasound and microbubbles.

3.1.2 Ultrasound and microbubble treatment

The treatment setup is shown in Figure 14. The mice were given anesthesia via an inhalation tube during the treatments. A tail vein catheter was used to administer nanoparticles and microbubbles. The leg containing the tumor was submerged in water, as illustrated, and the mouse was lying on a plate absorbing acoustic radiation. The water and mouse was kept warm using an aquarium heater and a heating lamp respectively (not illustrated). The ultrasound transducer (Imasonic SAS) was connected to a signal generator (33500 B, Keysight Technologies) and an amplifier(2100 L, Electronics and Innovations Ltd.), also not illustrated.

The treatment

All mice were anesthesized using 2.5% isofluorane in 1 L/min medical air. Pefore any treatment, all mice were given 200 µg of nanoparticles in 50 µL Dulbecco's phosphate-buffered saline (D-PBS) through the tail-vein catheter.

Five of the mice were given an ultrasound treatment. 50 µL of SonoVue were injected. The tumors were then sonicated for 9 minutes with a 1Mhz transducer. A burst period of 4 seconds and pulse length of 10 ms (10000 cycles) were used. The pulse repetition frequency was 0.25 Hz, resulting in a duty cycle of 0.25 %. The mechanical index was 0.5. After 3 and 6 minutes, a new dose of 50 µL SonoVue was given.

Five mice were used for control, they were injected with 50 µL of sonovue every 3 minutes for 9 minutes, no sonication using ultrasound was performed.

All of the mice woke up from anesthesia after treatment. 1 hour after finished treatment the mice were euthanized. The tumors were then taken out, then weighed and measured before being embedded in OCT Tissue Tek, and then submerged in liquid nitrogen.

2. The cells were grown and implanted by Caroline Einen.

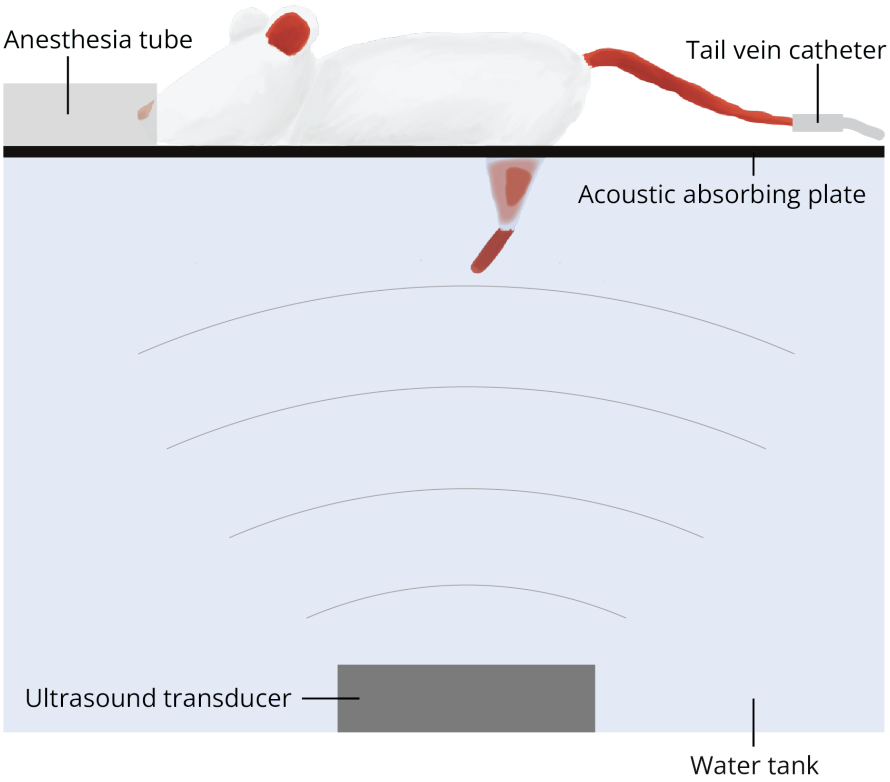

Figure 14: Illustration showing the treatment setup. The mouse is lying on a plate that can absorb acoustic waves. Through a hole in the plate, the leg containing the tumor is submerged in water. At the bottom of the water tank is an ultrasound transducer, delivering ultrasound to the tumor. The mouse is given anesthesia through an inhalation tube, and microbubbles and nanoparticles is administered through a tail vein catheter. Not included in the illustration is the signal generator and amplifier connected to the ultrasound transducer. The water was kept warm using an aquarium heater, and the mouse was kept warm through a heat lamp. The latter two components are also not illustrated.

Sectioning and HES imaging

The frozen tumors were cut in a cryostat, by the Cellular and Molecular Imaging Core facility (CMIC) at NTNU. The tumors were cut in three different levels. Level 1 was taken 500 µm from the tumor edge, there were 500 µm between level 1 and 2, and level 2 and 3. At each level the tumor was cut into two sections with 50 µm thickness, and 11 sections of 8 µm thickness. The sections were transferred to glass slides after cutting.

From each level, one section of 8 µm thickness was used for hematoxylin eosin saffron (HES) staining. The staining was done by CMIC. The HES sections were imaged using a Zeiss 800 Airyscan Confocal Microscope. Tilescans were acquired of the sections in bright field using a 10x Plan NeoFluar objective lens, with a numerical aperture of 0.3.

Imaging of the nanoparticles

To better localize the effects of microbubbles and ultrasound on the extracellular matrix, it was desirable to correlate the measured parameters in this thesis with the accumulation of nanoparticles. The aim was to do this by acquiring images of the tissue sections looking at the fluorescent signal from nanoparticles. Unfortunately, due to too little circulation time of the nanoparticles, they could not be imaged. This attempt was made by Charlotte Årseth, and more details can be found in her report.

3.2 Atomic force microscopy

The AFM used in this project was a BioScope Catalyst AFM from Bruker, integrated with an inverted Axio Observer Z1 from Zeiss. Nanoscope version 9.1 was used to control the Bioscope catalyst and acquire force distance curves using the "Force volume in fluid" mode.

3.2.1 Probe preparation and calibration

A probe with a spherical tip, with a diameter of 25 μm, from Novascan was used in the measurements, with a spring constant of 0.1 N/m according to the producer.

Hertz model assumes no attachment to the sample. Pluronic is a non-ionic copolymer surfactant, that makes surfaces hydrophobic. A 1% solution of Pluronic was prepared by incubating 1% (w/v) Pluronic in phosphate-buffered saline (PBS) at 37°C for 30 minutes. To minimize the attachment between the probe and the sample, the probe was prepared by soaking it in Pluronic for 45 minutes.

After soaking the probe in the Pluronic solution for 45 minutes, it was rinsed in D-PBS by moving the probe up and down in the solution.

After probe preparation, deflection sensitivity was calibrated by ramping (approaching and retracting from the surface once) on a glass slide with a droplet of D-PBS, and measuring the deflection sensitivity from the contact region of the resulting force distance curves. The probe was then withdrawn from the surface of the glass slide, and a thermal tune was done while the probe was still submerged in the D-PBS droplet. The thermal tune was done to calibrate the spring constant. This resulted in a spring constant of 0.07 ± 0.03 N/m on average, which is in accordance with the spring constant declared by the producer.

3.2.2 *Force curve acquisition*

The 50 µm thick sections were used for the AFM measurements. A droplet of D-PBS was put on the tissue sections to prevent the tissue from drying, and to provide a medium for measurements.

Prior to starting measurements, the location of the outermost edges of the tumor was found, and the maximum and minimum x and y coordinates were noted. From these coordinates, nine positions were found according to Figure 15, were position 2-5 were defined as peripheral positions, and the rest as central positions. At these positions, ten force distance curves were obtained by ramping in a grid pattern as shown in the figure. The distance between the measurement points in the grid was 7 µm.

The force distance curves were obtained by ramping with a ramp size of 10 µm, meaning that the distance between the probe and the sample before ramping is 10 µm. The approach and retract speed of the probe was 12 µm/s.

A total of 30 sections were used for the measurements, three sections from each tumor, one section per level.

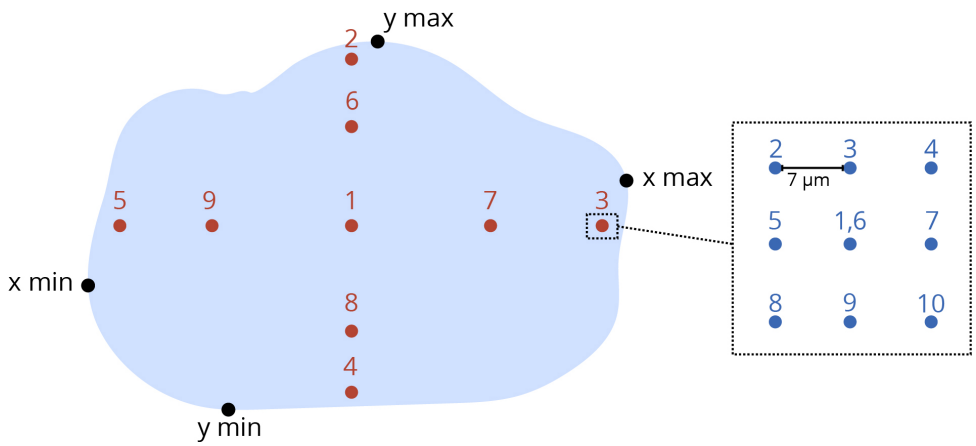

Figure 15: Illustrations showing the nine positions used for measurements per section (red dots), as well as the definition of x min and max, and y min and max, used to define the different positions. For each position, ten force distance curves were obtained in a grid, as shown in the inclusion. The distance between the measurements in the grid was 7 µm.

3.2.3 Curve fit analysis

As described in section 2.3.3, multiple algorithms exists for finding the contact point on an AFM force distance curve. To determine which algorithm was a better fit for the data obtained in this project, all of the four algorithms described in section 2.3.3 were tested on all the curves; goodness of fit, ΔE, ratio of variances and combined strategies. The resulting contact points were then used to calculate the Young's modulus, using Hertz model and a fit range starting from the contact point and ending at the end of the curve. Because the data set is fairly large ($\sim$ 2700 force distance curves), one can assume that the distribution of the Young's moduli from the various methods should be close to a normal distribution, according to the central limit theorem [42]. The algorithm that yielded the distribution of Young's moduli with the lowest skewness was therefore chosen as the algorithm used for all subsequent data analysis in this thesis.

Another parameter for the curve fit analysis is the fit range. A similar test as done for the contact point was done for three different fit ranges. One involved using the entire indentation depth, another used the first 50% of the total indentation depth and the third used only the last 50% of the total indentation depth. The combined strategies algorithm was used to determine the contact point for this analysis. Again, the fit range that yielded the distribution of Young's moduli with the lowest skewness was chosen as the indentation depth used for all data analysis in this thesis.

The result of the assessments can be found in subsection 4.1. Histograms of the different distributions was plotted, and statistical parameters was calculated using Graphpad Prism 9. The conclusion was that the best contact point algorithm was the combined strategies method. The most suitable fit range was determined to be the entire indentation depth.

Prior to curve fitting, the force curves were inspected to manually remove any faulty curves, i.e. force curves without a baseline or with substantial aberrations. The force distance curves were analyzed using a python script shown in Appendix A.

3.3 Multiphoton laser scanning microscopy

A Leica TCS SP8 confocal microscope equipped with a multiphoton (MP) laser was used for the collagen imaging based on the second harmonic signal. A condenser lens with a numerical aperture (NA) of 0.9 was used. The objective lens was a 20x Plan Apo magnification lens with a NA of 0.7. The LAS X software was used for image acquisition.

3.3.1 Sample preparation

The 8 µm thick sections were used for the SHG imaging. An 8 µL droplet of Vectashield® PLUS Antifade Mounting Medium (Vector Laboratories, H-1900) was added to the tumor section, and a coverglass was put on top.

3.3.2 Measurements

Prior to imaging, the microscope was adjusted for Köhler illumination. Tilescans of the tumor sections, in both forward and backward directions, were obtained simultaneously by using two separate detectors and an MP laser with a wavelength of 890nm and a laser power of 10%. The transmitted light detector was a PMT (photo multiplier tube) detector, and had a gain of 800V. The reflected light detector was a HyD (GaAsP) detector, and had a gain of 100%. Again, one section was measured per level per tumor, yielding a total of 30 sections measured. The built-in predictive 9 point focus map function in the LAS X software was used to focus the tilescans.

3.4 Data analysis

3.4.1 Image analysis

The SHG images were analyzed using ImageJ [43]. A region of interest (ROI) was established around the tumor, using the HES section images to omit any parts containing bright pink areas, which indicated muscle tissue. This is illustrated in Figure 16. The ROI was then split into a central and peripheral part. The peripheral part was defined as 10% of the length of the tumor. The center and periphery of the tumor is illustrated as yellow lines in Figure 16. A total of three ROIs are thus defined: the whole tumor, the tumor center and the tumor periphery.

The F/B ratio was calculated by using the "Image calculator" function, which divides two images with each other pixel by pixel. The function was used to divide the transmitted light image with the reflected light image, resulting in a F/B image. The F/B ratio was then obtained for the ROIs by measuring the mean gray value of the resulting F/B image.

The collagen density was estimated by calculating the collagen pixel area fraction in each image. A binary image was obtained by performing a triangle threshold on the image. This method of thresholding was chosen, as it produced the most consistent result. After thresholding, a median filter with a 2 pixel radius to remove background noise. The collagen density (in %) was then estimated by measuring the % of the area that included white pixels.

3.4.2 Correlation analysis between SHG and AFM data

The average central and peripheral values obtained per tumor was used from the AFM and SHG data to correlate the Young's modulus with the collagen density and F/B ratio. An attempt was made to correlate the AFM and SHG data more accurately, by superimposing the AFM coordinates with SHG tilescans taken of the same tissue sections as the AFM measurements. However, it was very hard to correlate the coordinates with the SHG tilescans properly. The images obtained of the collagen was not usable due to improper condenser lens position, so this correlation attempt is omitted from the rest of this report. The details and results of this attempt is outlined in Appendix B for future reference.

Correlation plots were also made between the tumor mass and average F/B ratio, collagen density and Young's modulus for each tumor.

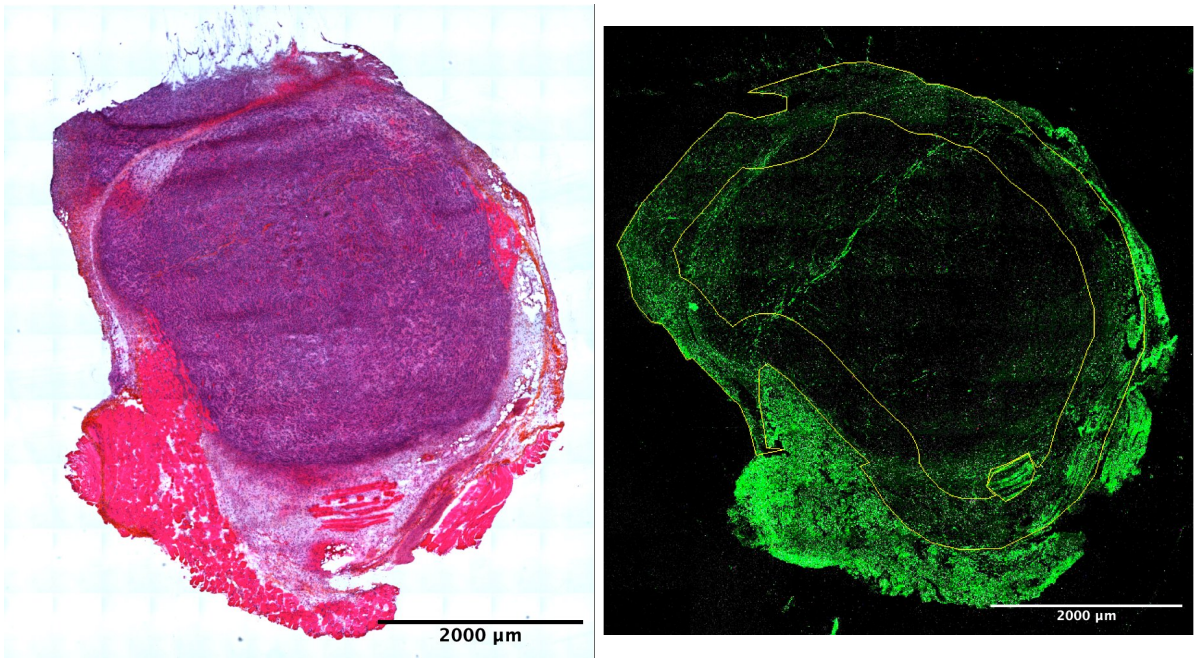

Figure 16: An example of an obtained tilescan image of an hematoxylin eosin saffron (HES) stained section (left), and a tilescan image of the same section obtained with second harmonic generation (SHG) microscopy (right). The brightness of both images have been increased for visualization purposes. The outermost yellow line in the SHG image marks the edge of the tumor, muscle tissue has been omitted (bright pink areas in the HES image). The area between the two yellow lines define the 10% margin, or the periphery. The remaining central area is defined as the tumor center.

3.4.3 Statistical analysis

All statistical analysis and plots were made in Graphpad Prism 9. To determine statistical significance, a normality test was first performed, to ensure that the data followed a Gaussian distribution. An unpaired, parametric t-test was then performed. For the correlation plots, correlation analysis was done to calculate Pearson r coefficient and significance. A simple linear regression line was also fitted to the correlation data. The statistical tests were deemed statistically significant for p-values less than or equal to 0.05. A Pearson r value between $\pm$ 0.1 and 0.3 is considered a small correlation, between $\pm$ 0.3 and 0.5 a medium correlation, and between $\pm$ 0.5 and 1 it is considered large.

Inter- vs intraheterogeneity

Several tests of inter- vs intraheterogeneity were done. A python script was used for calculation, and is included in Appendix C.

The heterogeneity of the AFM measurements were tested, by looking at the heterogeneity within the grid in Figure 15, defined as the intraheterogeneity. This heterogeneity was then compared to the heterogeneity between the positions, defined as the interheterogeneity. The inter- and interheterogeneity was calculated according subsection 2.5.

Intra- vs inter tumor heterogeneity was also calculated. This was done for the Young's modulus, the F/B ratio, and the collagen density. In this analysis, the heterogeneity within each tumor was then defined as the intraheterogeneity, while the interheterogeneity was defined as the heterogeneity between the tumors. For the Young's modulus, the intraheterogeneity was now defined as the heterogeneity between all of the positions measured within the same tumor.

4 RESULTS

4.1 Assessing curve fit parameters

4.1.1 Contact point

In Figure 17 is an example of a force curve, where the four different algorithms for finding the contact point, defined in subsubsection 2.3.3, have been used. Hertz model was used to estimate the Young's modulus for the different contact points, the entire indentation depth was used as the fit range. The different positions of the contact points are seen where the indentation depth is 0 on the x-axis, and where the fit with the Hertz model starts (orange curve). The resulting Young's modulus (E), and r^2 values are included. The example shows a typical situation, where the ΔE algorithm underestimated the contact point, while the Goodness of fit and Ratio of variances methods overestimated. However, this pattern did vary for some of the curves. More examples are included in Appendix D to illustrate the variation.

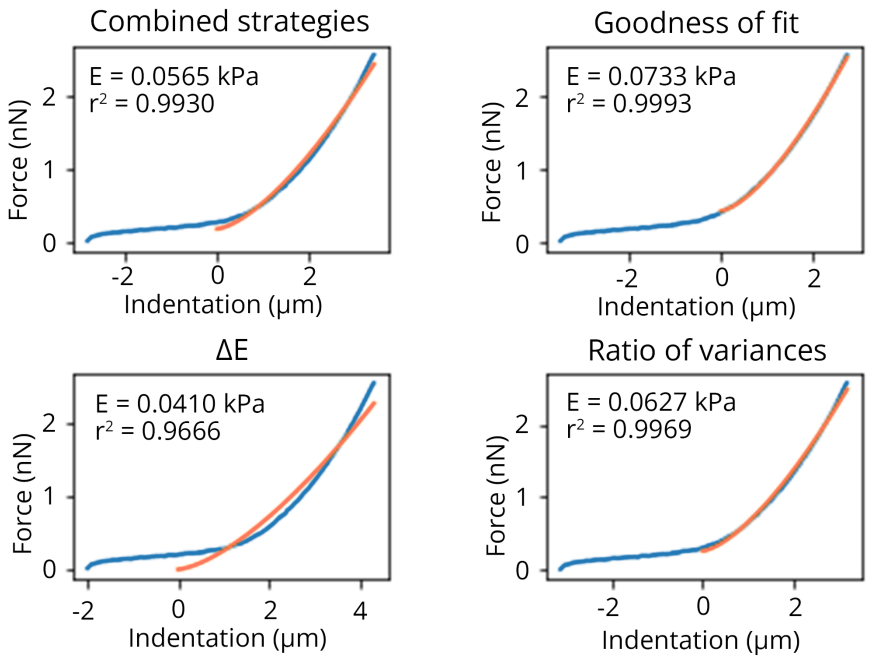

Figure 17: An example of a force curve, obtained with an atomic force microscope, and the result of using four different algorithms to calculate the location of the contact point. The fitted Hertz model is included in orange, and the resulting Young's modulus (E) and r^2 is shown in the upper left corner for each algorithm.

The resulting histograms of the Young's modulus values, obtained when using the different algorithms on 2703 curves, are shown in Figure 18. Note that the histogram is cut at 2 kPa to better asses the distribution, although some data points were above this. None of the curves showed a typical normal distribution. Table 1 shows statistics for the different algorithms, including maximum value, mean value, variance, and skewness. As can be seen from the table, the Combined strategies algorithm had the lowest skewness, and it is therefore the closest to a normal distribution.

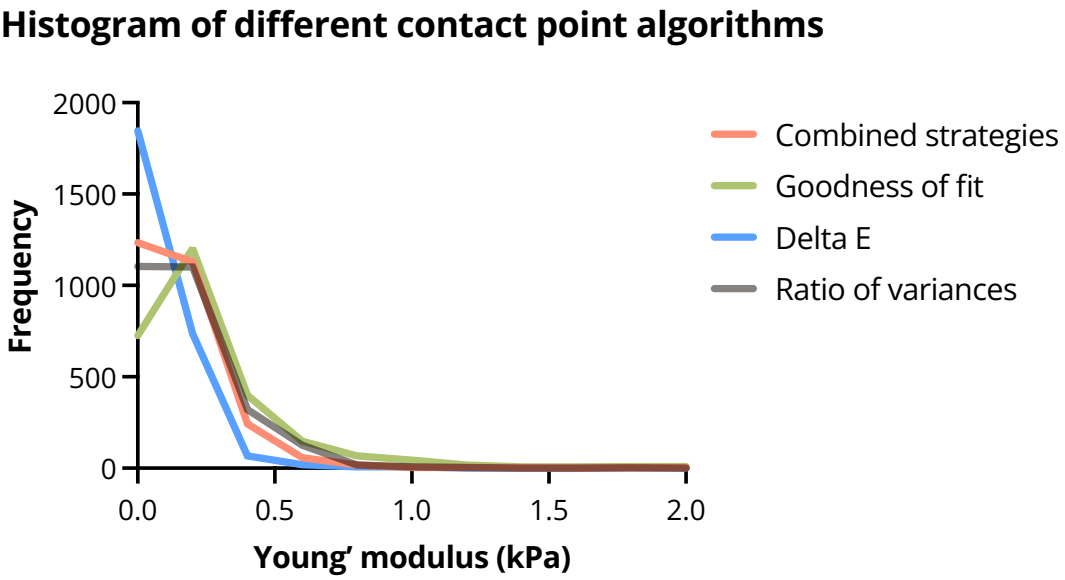

Figure 18: Histogram of the Young's modulus values obtained using the Hertz model on force curves when four different contact point algorithms have been used. The total number of values for each algorithm is ∼2700.

Table 1: Table showing statistical parameters of Young's modulus values obtained when four different contact point algorithms were used on 2703 force curves obtained using an AFM.

Algorithm	**Combined strategies**	**Goodness of fit**	**ΔE**	**Ratio of variances**
Maximum value (kPa)	2.249	56.42	4.047	7.693
Mean (kPa)	0.1606	0.3990	0.1005	0.2024
Variance (kPa^2)	0.0305	2.338	0.0264	0.116
Skewness	4.816	22.00	10.77	11.32

4.1.2 Fit range

Figure 19 shows an example of the same force curve as in Figure 17. Here, three different fit ranges has been used to estimate the Young's modulus, using Hertz model. The contact point was chosen according to the Combined strategies algorithm, and was used for the start of two of the fit ranges, as can be seen in the figure. The fit can be seen in orange, and the resulting Young's modulus (E) and r^2 values are included. This example shows a typical situation, where the fit range using only the last 50% of the curve gave the highest Young's modulus, the fit range using only the beginning 50% had the lowest, and using the entire indentation depth as a fit range gave a Young's modulus in between the other two.

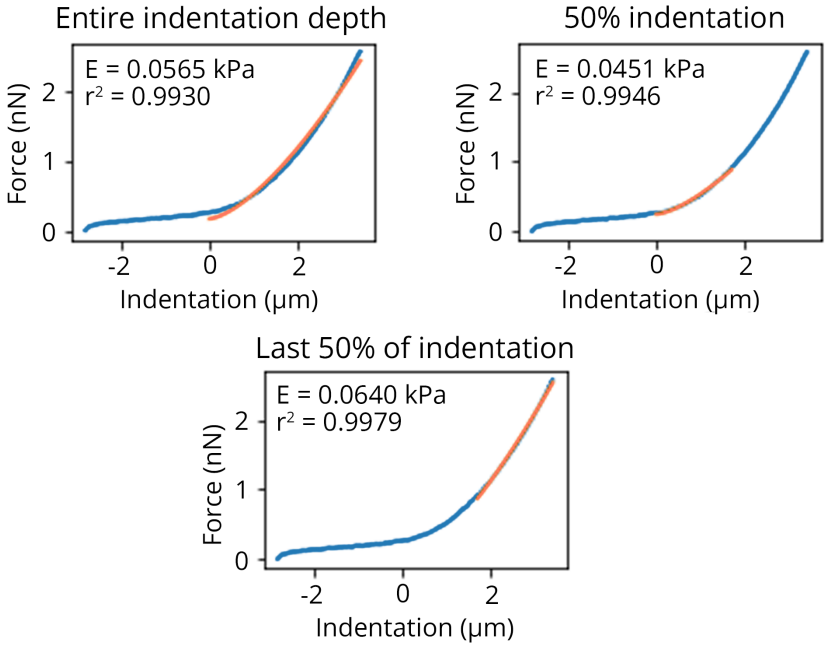

Figure 19: An example of a force curve obtained with an atomic force microscope, and the three different fit ranges used with the Hertz model. The fitted Hertz model is included in orange, and the resulting Young's modulus (E) and r^2 is shown in the upper left corner for each fit range.

Figure 20 shows the resulting histogram of the different Young's modulus values obtained with the different fit ranges for 2703 curves. Again, there was no obvious normal distribution for any of the curves. Table 2 shows maximum value, mean value, variance, and skewness for the different fit ranges. Using the entire indentation depth as a fit range yielded the lowest skewness. This was therefore chosen as the fit range, since it also includes all the information of the curve. The tissue section thickness of 50 µm is sufficiently thick to avoid substrate effects, as Buckles rule state that the indentation depth should be less than 5-10% of the sample thickness, and the indentation depth varied between 2 and 4 µm [34].

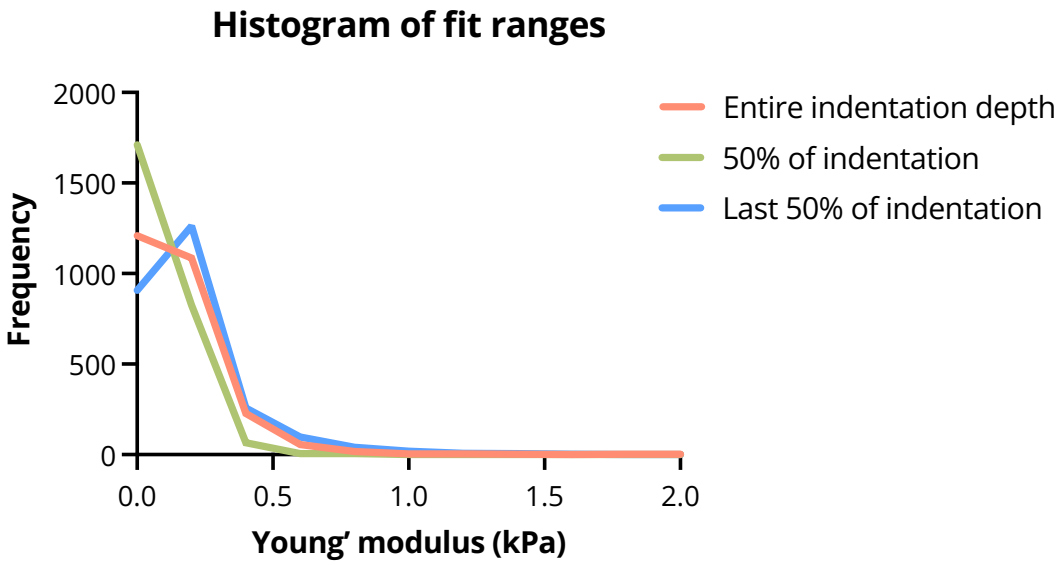

Figure 20: Histogram of the Young's modulus values obtained using the Hertz model on 2700 force curves with three different fit ranges.

Table 2: Table showing statistical parameters when three different fit ranges were used on 2703 curves. The Hertz model was used to estimate the Young's modulus for all curves.

Fit range	**Whole curve**	**50% indentation**	**Last 50% of indentation**
Maximum value	2.249	3.238	4.061
Mean	0.1606	0.0946	0.2084
Variance	0.0305	0.0119	0.0779
Skewness	4.816	10.83	6.660

4.2 Young's modulus

Figure 21 shows an example of a force curve obtained using the AFM on a 4T1 tissue section, including both the approach curve (blue) and retract curve (green). As can be seen from the figure there is a hysteresis between the two curves, indicating that the sample is viscoelastic.

Figure 22 shows the resulting Young's moduli in control (red) and treated (blue) tumors. The average Young's modulus was 0.15 ± 0.04 kPa for both the control and treated tumors. The bars show the mean value, and the error bars the standard deviation. Each data point represent the average Young's modulus of each tumor, which is the average of three tumor sections. For the "Total" plot, each tumor section is the average of nine positions, which again is the average of ten measurements each. For the center and periphery, each tumor section is the average of five and four positions respectively. No statistical significant difference were found between the Young's moduli in control and treated tumors in any of the plots. There were also no statistical significant difference between center and periphery measurements, but there is a slight trend for the tumor periphery to be stiffer than the tumor center.

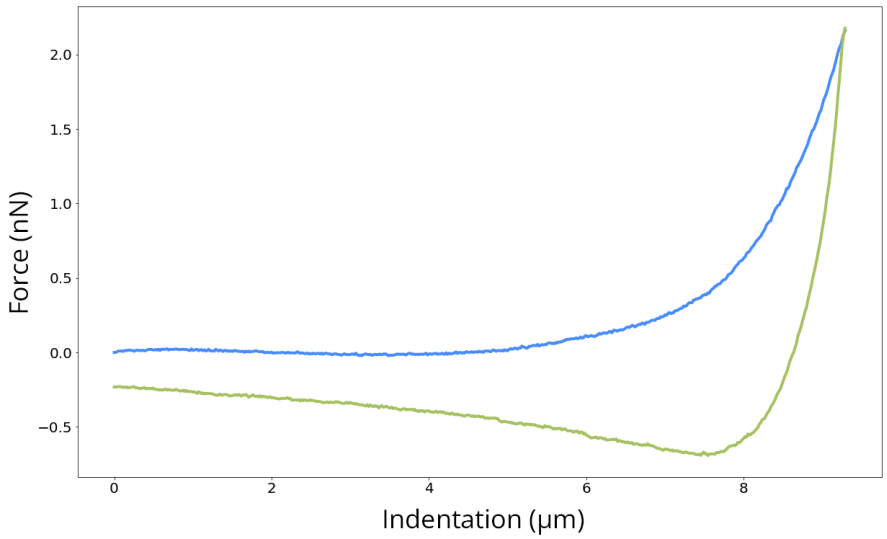

Figure 21: A force distance curved obtained on a 4T1 tissue section using an atomic force microscope. The approach and retract curves are shown in blue and green respectively.

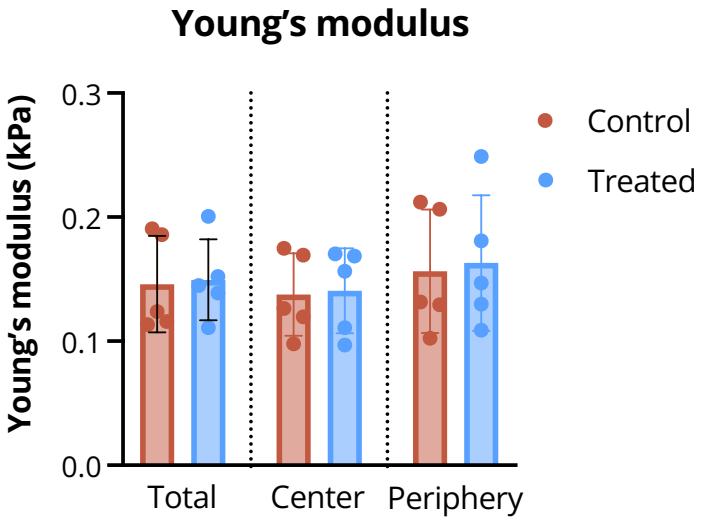

Figure 22: Scatter bar plot showing the resulting Young's moduli in treated and control 4T1 tumors. The bars show the mean value, and the error bars the standard deviation. Each data point represent the average Young's modulus found for each tumor, which the average value obtained from three tumor sections. The average Young's modulus found in the center and periphery of each tumor is also included. No statistical significance was found between any of the columns.

The inter- versus intraheterogeneity test performed, showed that the interheterogeneity, the heterogeneity between the different positions on the sample, was higher than the heterogeneity within the position. The inter- and intraheterogeneity was 0.025 kPa^2 and 0.014 kPa^2 respectively. Thus, the relative contribution of intraheterogeneity, f, was 0.36, which is less than 0.5. This means that the contribution of the intraheterogeneity to the total heterogeneity is less than the contribution of the interheterogeneity.

4.3 Second harmonic generation microscopy

There was a large variation in the F/B ratio obtained from different tumors. The highest and lowest obtained F/B ratios were 3.1 and 1.2 respectively. Figure 23 shows tilescans obtained using second harmonic generation microscopy of the tissue section having the highest F/B ratio . Figure 24 shows tilescans of the tissue section with the lowest F/B ratio. For both tissue sections, a) shows the resulting tilescan from the forward signal, and b) from the backwards signal. c) and d) shows a closeup from the same tilescans, in the forward and backwards directions respectively. As can be seen in the images, the tissue section with the highest F/B ratio has a substantially higher signal in both the forward and backward channel, compared to the tilescan of the tissue section with the lowest F/B ratio. In the latter, the signal is almost invisible. As can be seen in closeup images for both tissue sections, both the forward and backward signal shows the same structures, but the signal intensity is higher for the forward channel.

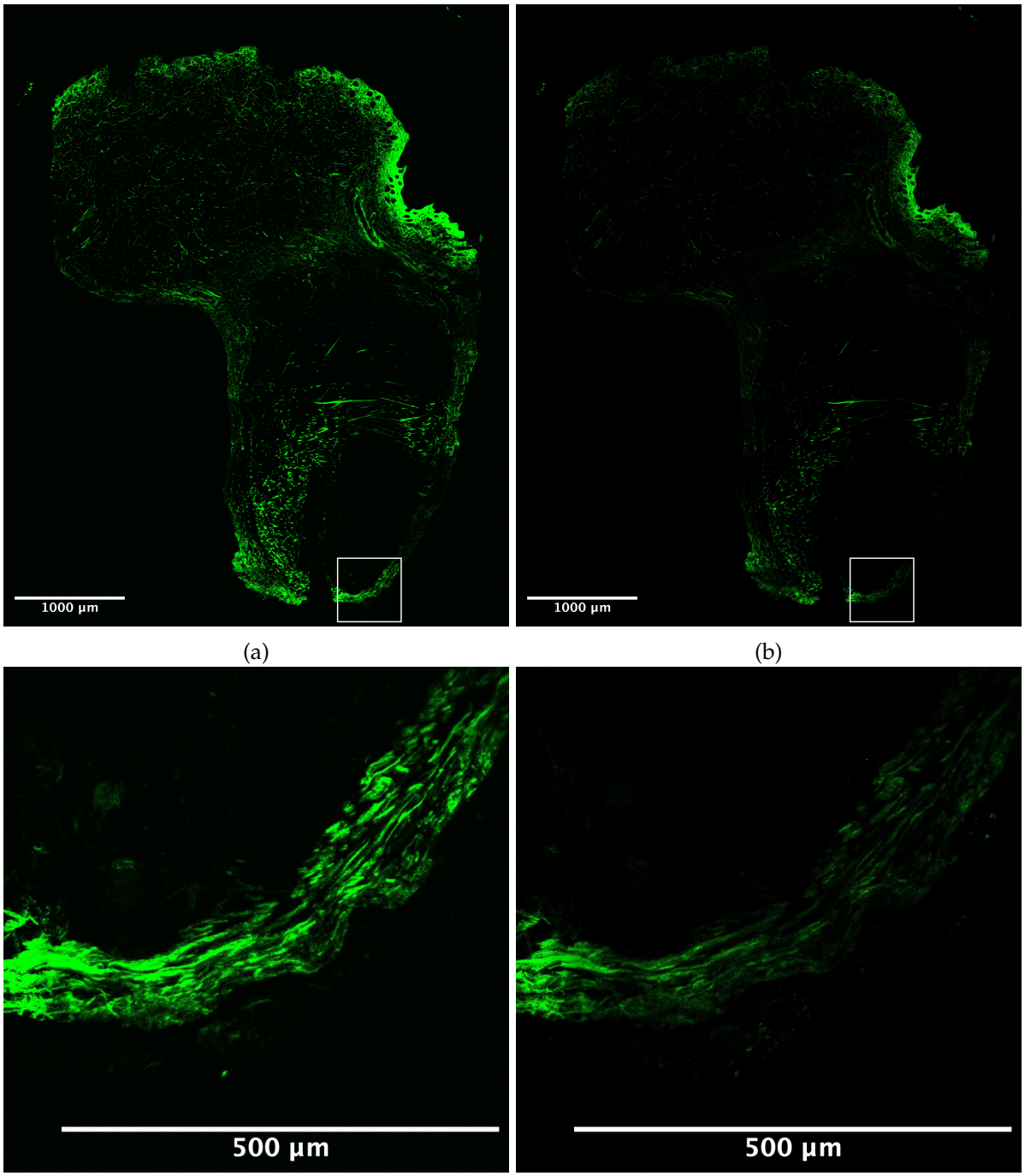

(a) (b)

(c) (d)

Figure 23: A tilescan image obtained using second harmonic generation (SHG) microscopy, from a 4T1 tissue section with a resulting forward to backward ratio of 3.1. Collagen is shown in green. a) Shows the image obtained in the forward channel, b) in the backwards channel. c) and d) are closeup of the highlighted region in a) and b) respectively.

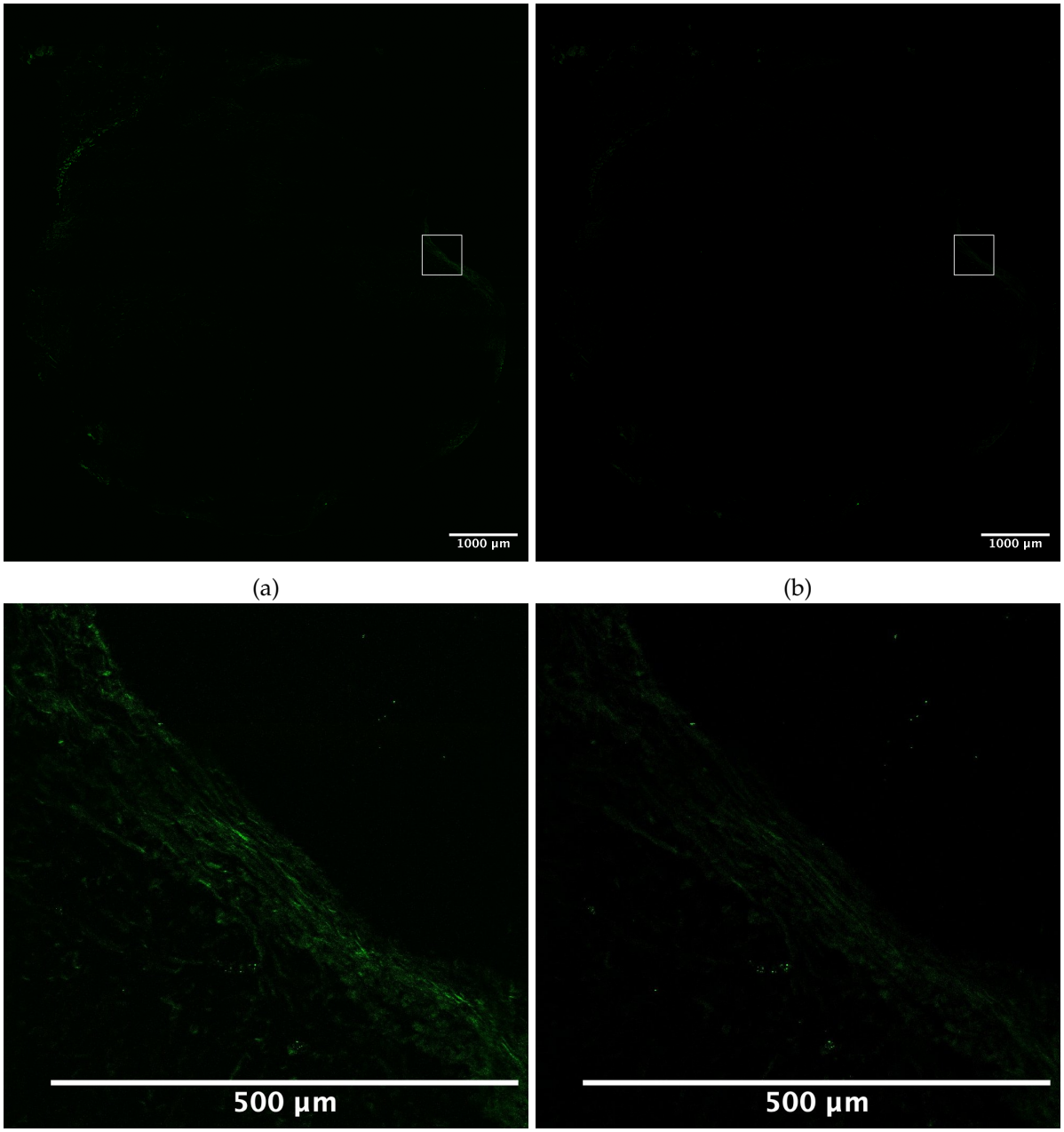

(a) (b)

(c) (d)

Figure 24: A tilescan image obtained using second harmonic generation (SHG) microscopy, from a 4T1 tissue section with a forward to backward ratio of 1.2. Collagen is shown in green. a) Shows the image obtained in the forward channel, b) in the backwards channel. c) and d) are closeup of the highlighted region in a) and b) respectively.

A large variation was also found in the collagen density between tumors. The highest and lowest collagen density was 23.9% and 1.2% respectively. Figure 25 shows tilescans, from the forward channel, of two tumor sections before and after thresholding and median filtering. a) and b) is from the tissue section yielding the highest collagen density, note that this is the same section as in Figure 23. c) and d) is from the tissue section resulting in the lowest collagen density. The bright features on the right of Figure 25d stem from muscle tissue, and has not been included when calculating the collagen density.

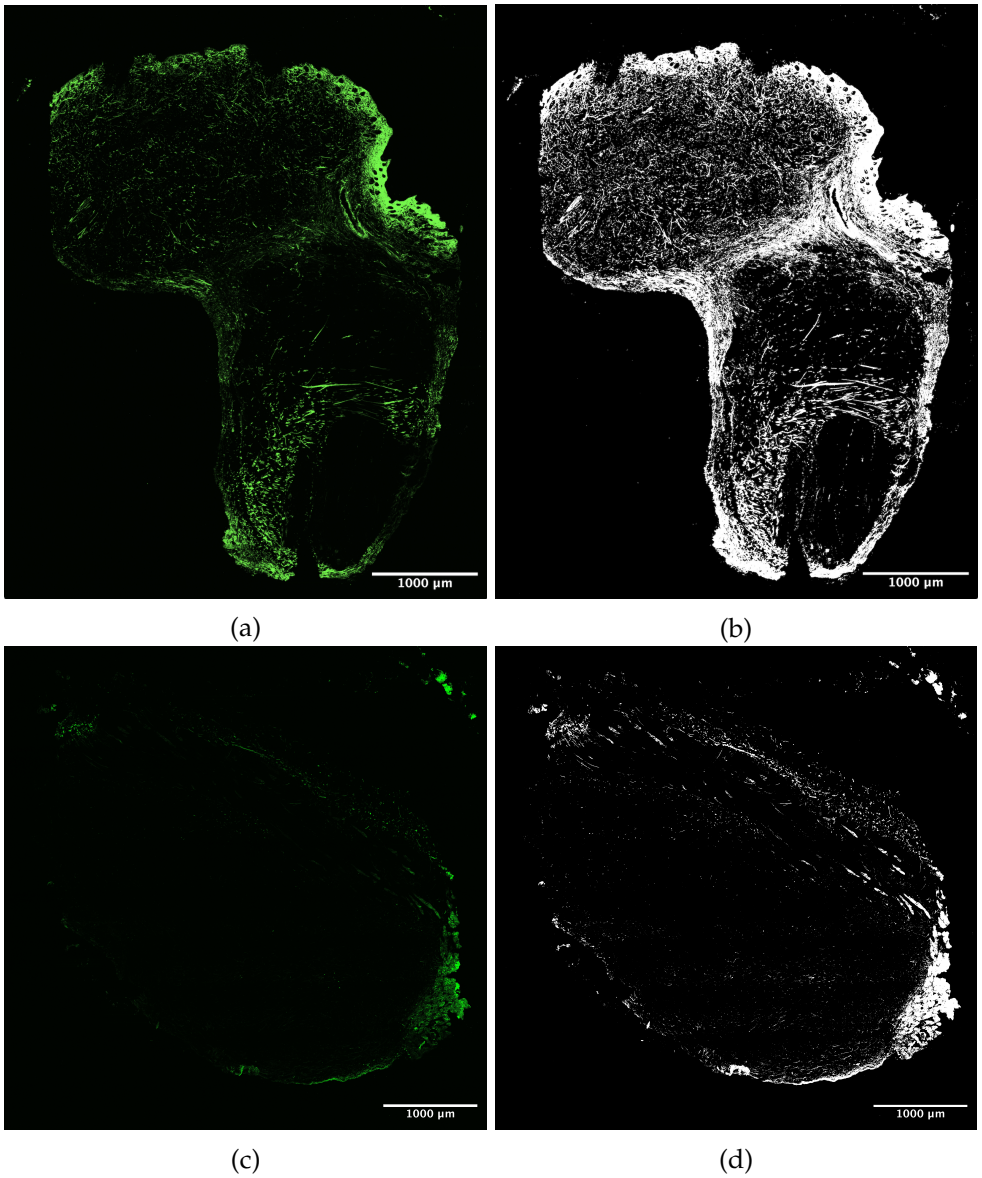

Figure 25: Tilescan images obtained using second harmonic generation (SHG) microscopy in the forward direction, before (a and c), and after (b and d), triangle thresholding and median filtering. a),b) is a tilescan from the tissue section with the highest measured collagen density. c),d) is from the tissue section with the lowest measured collagen density. The highest and lowest collagen density was 23.9% and 1.2% respectively. The bright features in (d) stem from muscle tissue and has not been included when calculating the collagen density.

Figure 26 shows scatter bar plots of the F/B ratio and collagen density. The bars mark the mean, and the error bars the standard deviation. The plots compare the values for the control and treated tumors, and the periphery and central values have been separated. Each data point represents the average value found for each tumor, obtained from three tissue sections. The plots show no difference between control and treated tumors. The average F/B ratio was 1.7 ± 0.23 for the control tumors and 1.8 ± 0.34 for the treated tumors. For the collagen density, the average values were 6.5 ± 2.3 % and 6.6 ± 3.1%, for the control and treated tumors respectively.

There is a tendency for both the F/B ratio and the collagen density to be higher in the periphery than in the center of the tumor. For the F/B ratio, the average center and periphery values for the control tumors were 1.5 ± 0.28 and 1.8 ± 0.31 respectively. For the treated tumors, they were 1.5 ± 0.29 and 1.9 ± 0.34. For the collagen density, the average center and periphery values were 4.4 ± 1.9% and 9.3 ± 3.0% for the control tumors, and 3.6 ± 1.8% and 9.9 ± 4.5% for the treated tumors. This difference is statistically significant for the collagen density in the treated tumors. The treated outlier visible in the collagen density plot, is the same outlier as in Figure 22, and is the section shown in Figure 23 and 25a) and b).

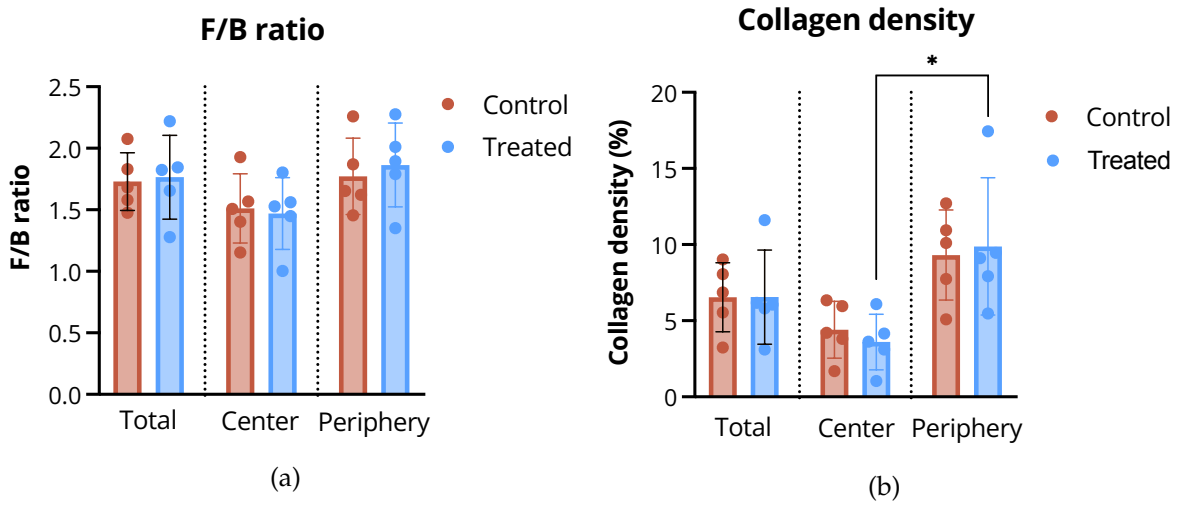

Figure 26: Scatter bar plots showing the resulting F/B ratio (a) and collagen density (b) in treated and untreated 4T1 tumors. The bars show the mean value, and the error bars the standard deviation. Each data point represent the average F/B ratio or collagen density found for each tumor, which is the average from three tumor sections. The average F/B ratio and collagen density found in the center and periphery of each tumor are also included. A statistical significance was found between the center and periphery for the collagen density in the treated tumors, no statistical significance was found between any other columns. * = $p < 0.05$.

4.4 Correlation between collagen and Young's modulus

Figure 27 shows the scatter plots of the Young's modulus and F/B ratio. Figure 28 shows the scatter plots of the Young's modulus and collagen density. Each data point represents the average Young's modulus and F/B ratio, or collagen density, in either the center or periphery of each tumor, indicated by a closed or open circle respectively. The red data points represents the values obtained for the control tumors, and the blue the treated tumors. A regression line is included, it is calculated for all the data points, regardless of whether the tumor is control or treated, since there was no statistical difference between the two groups.

As can be seen from the regression line in Figure 27, there is a trend for the F/B ratio to increase with increasing Young's modulus. The Pearson r coefficient is 0.37, which signifies a medium correlation. However, the p value is 0.1, which means that the correlation is not statistically significant.

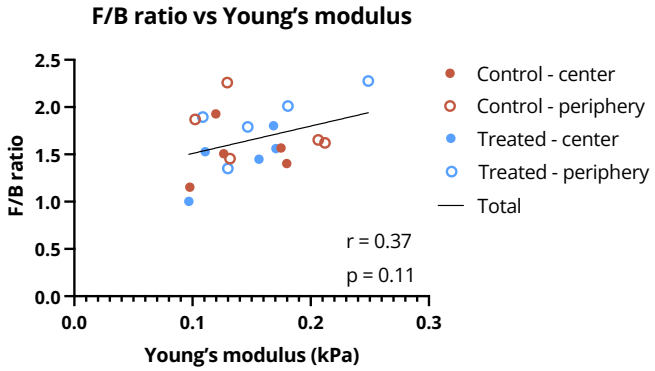

Figure 27: Scatter plot showing the correlation between Young's modulus and F/B ratio of control (red) and treated (blue) 4T1 tumors. Each data point represents either the average center or peripheral average value for each tumor, indicated by a closed or open circle respectively. The black regression line is calculated for all data points regardless of whether the tumor has been treated or is a control. The correlation analysis found a Pearson r coefficient of 0.37 and a p value of 0.1, which is not statistically significant.

The regression line in Figure 28 shows that there is a trend for the collagen density to increase with an increasing Young's modulus. Here, the Pearson r coefficient is 0.55 and the p value is 0.01. This means that the correlation is medium large, and that the trend is statistically significant.

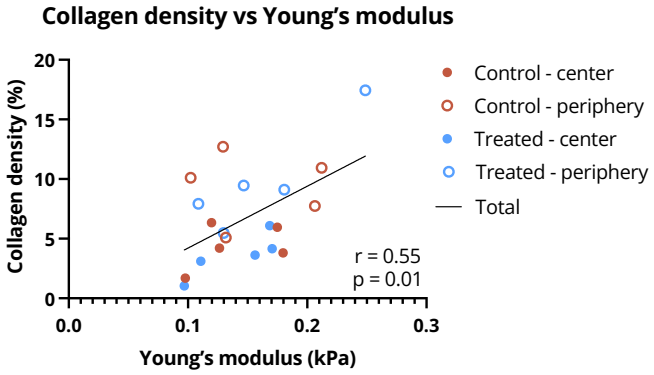

Figure 28: Scatter plot showing the correlation between Young's modulus and collagen density of control (red) and treated (blue) 4T1 tumors. Each data point represents the average of either the center or peripheral value for each tumor, indicated by a closed or open circle respectively. The black regression line is calculated for all data points regardless of whether the tumor has been treated or is a control. The correlation analysis found a Pearson r coefficient of 0.55 and a p value of 0.01, which is statistically significant.

4.5 Correlation between tumor mass and experimental parameters

Figure 29 shows the scatter plots of tumor mass and Young's modulus (a), F/B ratio (b) and collagen density (c). The red data points represents control tumors, and the blue the treated tumors. A regression line calculated for all data points is also included. As can be seen from the plots there is a medium negative correlation between tumor mass and the Young's modulus, and a small negative correlation between tumor mass and F/B ratio and collagen density. However, the correlation is not statistically significant for any of the plots.

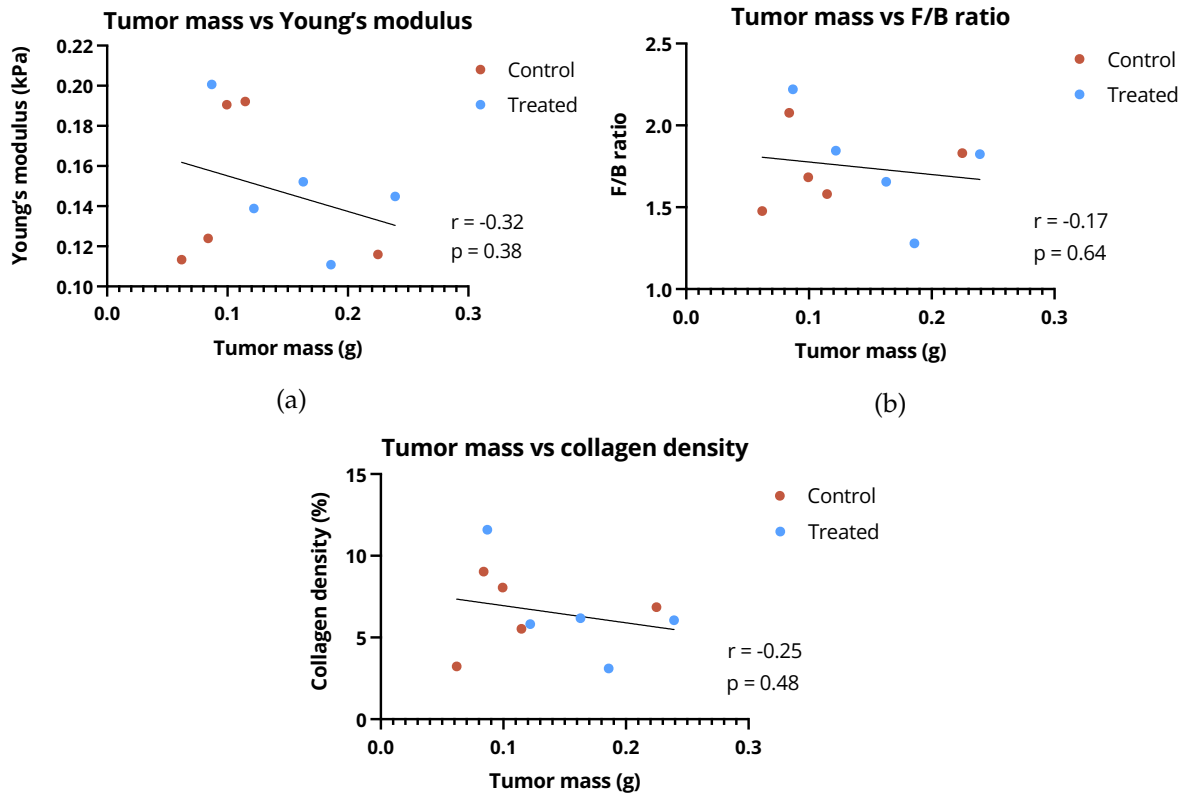

Figure 29: Scatter plot showing the correlation between tumor mass and Young's modulus (a), F/B ratio (b) and collagen density (c), of control (red) and treated (blue) 4T1 tumors. Each data point represents the mass and average measured parameter per tumor. The black regression line is calculated for all data points regardless of whether the tumor has been treated or is a control. The correlation analysis found a weak negative correlation for all plots, but no statistical significance. The Pearson r and p values are included in the lower right corners of all plots.

4.6 Inter- vs intratumor heterogeneity

Table 3 shows the inter- and intratumor heterogeneity, explained in section 2.5, as well as the relative contribution of the intratumor heterogeneity on the total heterogeneity, f, for the measured Young's modulus, F/B ratio and collagen density. As can be from the f values in the table, all the different parameters have a stronger intertumor heterogeneity than intratumor heterogeneity. The relative contribution of the intra tumorheterogeneity is still quite large, especially for the measured Young's modulus and collagen density. This means that the variation measured within each tumor is almost as large as the variation measured between tumors.

Table 3: Table showing the intertumor heterogeneity (σ^2_{inter}) and intratumor heterogeneity (σ^2_{intra}) for each measured parameter. The f value signifies the relative contribution of the intratumorheterogeneity to the total heterogeneity of the sample population.

Measured property	σ^2_{inter}	σ^2_{intra}	**f**
Young's modulus	0.011	0.010	0.47
F/B ratio	0.158	0.090	0.36
Collagen density	20.8	14.9	0.42

5 Discussion

5.1 Contact point and fit range assessment

In this project it was concluded that the combined strategies method was the best algorithm for calculating the contact point, based on both manual inspection of randomly chosen curves and statistical analysis. This was the same conclusion made by Gavara (2016) [37], whose work this contact point assessment was based on. They also evaluated the algorithms based on statistics. However, their experiments were done on hydrogels with a known stiffness.

As can be seen from Figure 18, the distributions were not very close to normal for any of the algorithms. Since a heterogeneous sample was used, this might not be entirely unexpected. It was therefore important to support the statistical analysis with a manual inspection of some of the curves. From this it was visible that the combined strategies yielded the best results.

The distributions obtained by different fit ranges, shown in Figure 20, shows similar distributions to what was found for the contact point algorithms in Figure 18. Again, none of the distributions were close to normal. The decision of using the entire indentation depth was therefore supported by the fact that this would include all of the information on the curve.

It is interesting to note that using the last 50% of indentation has a very similar distribution to the Goodness of fit method, supporting the notion that this algorithm overestimated the position of the contact point.

5.2 Young's modulus, F/B ratio and collagen area fraction of 4T1 tumors in literature

Young's modulus

While many studies have measured the Young's modulus of single 4T1 cells, very few have looked into the Young's modulus on tumor sections. Rao et al. (2019) measured the stiffness of orthotopic 4T1 tumors. They used a macroscopic indentation device with a 2 mm cylindrical probe and found average Young's modulus of ~ 7 kPa [44] for their control tumors. Another study, conducted by Riegler et al. (2018), used an unconfined compression method, on orthotopic 4T1 tumors, and found an average Young's modulus of ~ 50 kPa [45]. This shows that the Young's modulus is heavily dependent on the method used. One study that used the AFM to measure Young's modulus in 4T1 tumors was found. This study, done by Voutouri et al. (2021), found an average Young's modulus of ~ 4.5 kPa for their control tumors [46]. In this project, the average Young's modulus was 0.15 kPa, which is lower than what Voutouri et al. found. There are however many differences between their study and this project. First of all, their study was done on an orhtotopic tumor model, and not a subcutaneous model such as in this thesis. Second, the measurements were done on samples that hadn't been frozen. Other studies on the effect on stiffness of freezing/thawing tissue before measurements have shown a decrease in Young's modulus compared to fresh samples [47, 48]. Lastly, the AFM measurements were done by force mapping with

a pyramidal tip with a 20 nm tip radius. A study done by Sicard et al. (2017) on pulmonary arterial tissue stiffness, acquired the Young's modulus using the AFM. They compared the values obtained with a spherical tip with those obtained with a pyramidal tip, and found that the pyramidal tip gave almost ten times higher Young's modulus values [49]. This means that when comparing the study by Voutouri et al.[46] with this project, there are two major difference that could have a large impact on obtained Young's modulus: the frozen versus fresh sections, and the tip geometry.

The comparisons with different literature values doesn't give any validation for the obtained Young's modulus results in this thesis. It does however show that the Young's modulus should not be regarded as an absolute value, as it varies greatly with the experimental method. By keeping the method constant, which was done in this thesis, it is suitable for comparing stiffness changes between control and treated samples.

F/B ratio

A study done by Han et al. (2008) on 4T1 tumor tissue found an F/B ratio of 44.5 $\pm$ 15 [50], which is much higher than the F/B ratio of 1.75 $\pm$ 0.28 found in this project. However, there is one major limitation to the measurements done in this project. The two detectors used for forward and backward signal detection are different. The HyD detector used for the backward signal is in general more sensitive than the PMT detector used for the forward signal. Therefore, in order to get results comparable to those found in literature, a calibration step, using fluorescent polystyrene beads, should have been performed. However, since the main focus in this project are the relative values, this was not done. In future work this should however be done, as it yields comparable results between different studies, which may be valuable and make the research more reproducible.

Collagen area fraction

No studies were found that looked at collagen area fraction in 4T1 tumors using SHG. However, two studies, done by Polydorou et al. (2017) and Voutouri et al. (2018) respectively, looked at the collagen area fraction in 4T1 tumors using fluorescent immunohistochemistry. They both found a collagen area fraction of $\sim$ 65% [46, 51].The average collagen area fraction found in this project was 6.5%, which is ten times lower. It should however be noted that detecting collagen by staining is not reliant on either the collagen structure or orientation, compared to SHG. It is also possible to stain smaller fibrils that would not be detectable with the SHG. This might help explain the big difference. The SHG is however advantageous to staining as it is a label free technique, and is it possible to assess the organization via the F/B ratio.

A study done by Sulheim et al. (2018) looked at the area fraction using SHG in five different tumor models: two different prostate cancer cell lines, PC3 and PC3/2G7, OHS osteosarcoma, MDA-MB-231 breast cancer and A431 epidermoid carcinoma. They found the collagen density to be highly variable, varying from 0 to over 10%. The area fraction varied between the different tumor models, where the A431 had significantly lower collagen density compared to the PC3 model. The breast cancer model had an average area fraction of $\sim 4\%$ [52]. The collagen density values found in this project are within the range of values found by Sulheim et al. in their study, using the same technique.

5.3 Tumor heterogeneity

As can be seen from Figure 22 and 26, there is a large variation between tumors. This is not unexpected, as tumors are complex tissues and grow at different rates. This is evident from the large variation in tumor mass, as seen in Figure 29, even though the time from implantation to excision was the same for all tumors. From the inter- versus intraheterogeneity analysis, it seems that some of the apparent variations also stem from between the different tumor sections of each tumor. This is evident in the high relative contribution of intratumor heterogeneity, especially for the Young's modulus and the collagen density. As both inter- and intratumor heterogeneity has implications on prognosis, it is a well known concept. Intratumor heterogeneity stems from a heterogeneous cell population, and has been observed in a several different cancer types, including breast tumors. The high intratumor heterogeneity observed in this project is therefore not unexpected, especially since the different tumor sections were taken from different levels. [53, 54]

For the Young's modulus, this large intratumor variation is not suprising, as it is very dependent on the positions of the measurements. The contact diameter of a probe is given by the equation $R_c = 2\sqrt{R\delta - \frac{\delta}{4}}$ [34]. For a probe with a radius of 12.5 $\mu\mathrm{m}$, and an average indentation depth of 2.5 $\mu\mathrm{m}$, this would result in a contact diameter of 11 $\mu\mathrm{m}$. With a step size of 7 $\mu\mathrm{m}$, the total size of the measured grid per position would be 25 by 25 $\mu\mathrm{m}$. Collagen fibers can be up to 20 $\mu\mathrm{m}$ in diameter [55], and some breast cancer cell lines can be up to 15 $\mu\mathrm{m}$ in diameter [56]. This means that a large fraction of the measurements in the grid can come from singular components such as cells or collagen. This would result in large differences in Young's moduli between positions, as a collagen fiber is stiffer than a cell [56]. This notion is supported by the fact that the heterogeneity within each grid is lower than between the different positions, which means that some of the measurements within the grid most likely are done on similar structures.

For the collagen measurements, it should also be noted that the focus map function in LAS X is not perfect, and in some tilescans there are visible darker spots that seems to be due to the image being out of focus, and not because of low collagen density. In both Figure 24 and Figure 25c and 25d, the images are quite dark, which could be due to bad focus. This could of course also further decrease the obtained value for collagen area fraction and F/B ratio. This is one of the limitations of this project that can also affect the relative results, as some tilescans might have more areas that are out of focus than others. The significance of this difference is however somewhat minimized by having three sections imaged per tumor. And, as there is a strong correlation between Young's modulus and the collagen density (discussed more below), it is likely that this wasn't a major issue.

5.4 Control versus treated samples

No significant difference was found between control and treated tumors for any of the parameters measured in this project, suggesting that the ultrasound and microbubble treatment does not affect the collagen in terms of density or organization, nor does it affect the tumor stiffness, at least not detectable with the used methods.

No difference was found between the Young's modulus in control and treated tumors. This was the same result Sulheim et al. (2021) got when looking at differences in OHS osteosarcomas and PC3 prostate tumors before and after treatment with ultrasound and microbubbles. They used a macro compression method with a 2.5 mm indenter radius [57].

In regards to collagen, a similar study done by Zhang et al. (2019) came to the same conclusion. They tested the effect on VX2 tumors in rabbits of nonfocused, low-frequency ultrasound, with and without microbubbles, and at different acoustic pressures. The peak negative pressure ranged from 1 to 5 MPa. In this project, a mechanical index of 0.5 was used with a frequency of 1MHz. According to Equation 5, this results in a peak negative preasure of 0.5 MPa, which is lower than the pressures used in the study by Zhang et al. They used Masson Staining to look at the collagen content at ten random field-of-views in the tumor sections. They also found no difference between control and treated groups [58]. The acoustic pressure is related to intensity, and a pressure of 1MPa is considered low intensity ultrasound, while a pressure of 5MPa is considered high intensity. However, these high intensities are not clinically relevant for drug delivery. The clinical relevance is the reasoning behind the low intensity used in this project.

Other studies using even higher intensity ultrasound did find changes between control and treated groups. Li et al. (2015) and Lee et al. (2017) both looked at the collagen using Masson staining in KPC tumors, and SCC7 and A549 tumors, respectively. The tumors were treated with pulsed high intensity focused ultrasound (pHIFU), without microbubbles, in both studies. Both studies found disruption of collagen fibers in their treated animals [59, 60]. This implies that the effect of ultrasound on tissue is highly dependent on the ultrasound intensity.

There is one limitation to both this project and the study done by Zhang et al. Unlike HIFU which is meant to affect the entire tumor tissue, our methods relies on the activation of microbubbles, and it is the microbubbles in combination with ultrasound that might have an effect. Since the microbubbles only are present in perfused blood vessels, the potential effect would most likely be very limited to the area around these vessels. It is expected that the oscillation of the microbubbles would cause an oscillation of the blood vessel wall, which would in turn cause an oscillation of the ECM fibers in contact with the blood vessel wall. Any alterations in the ECM would therefore be very localized. Therefore, imaging the entire tumor and taking the average value to determine the effect of the treatment would yield varying results, as it would be highly dependent on the density of perfused vessels in the tumors during treatment. As the effects would be very localized, a more localized and directed imaging, or analysis, method should be employed. This could for instance include looking at the collagen content, and orientation, in relation to perfused blood vessels (for example via FITC staining) and accumulation of nanoparticles, as it is assumed that these would accumulate in the vacancy of microbubbles. One could then see how, or if, the collagen content, orientation or stiffness change as a function of distance from these areas. These changes can then be compared between treated and untreated tumors.

When it comes to the measurements of stiffness using the AFM, another problem is encountered. While the AFM is very localized, it is not aimed at certain locations in any way. The choice of positions is completely random. A way of making more use of these measurements would be to correlate them with the SHG tilescans. This way one could understand what the underlying substrate of the measurements were. By again also imaging the nanoparticle accumulation and FITC signal from perfused blood vessels, one could relate the AFM measurements to the tissue around activated microbubbles. As mentioned in section 3.4.2, a failed attempt of this was made by superimposing the AFM coordinates with the SHG tilescan, the details of which can be read in Appendix B. Another, maybe more succesful, approach would be to perform the measurements at interesting locations, instead of trying to find out what was measured after the fact. The Axio Observer Z1 from Zeiss is an epifluorescence microscope, capable of imaging both FITC signal and signal from fluorescent nanoparticles. This means that the positioning of the AFM can be chosen in relation to the perfused blood vessels and nanoparticles. There are however one possible limitation to this, since it is an epifluorescence microscope and not a confocal laser scanning microscope, there is no optical sectioning. This would mean that the signal through a 50 μm section could contain substantial background noise. It should however make it easier to aim the measurements at interesting locations than when looking at the sample only in brightfield. By imaging both the AFM positions and the tilescans using the FITC and nanoparticle signal, the superimposition of the two images might be easier. This could in turn help make the correlation between the data more precise.

5.5 Correlations

Young's modulus versus collagen area fraction

As can be seen in Figure 28 there is a correlation between the measured Young's modulus and collagen area fraction. There is a significant trend for the measured Young's modulus to increase with higher collagen content. This is as expected as the increased collagen density is recognized as a major contribution to increased tumor stiffness [2, 45, 61, 62].

Young's modulus versus F/B ratio

A slight trend can be seen in Figure 27 for the F/B ratio to increase with increasing stiffness, albeit not statistically significant. A study done by Chu et al. (2007) found a correlation between F/B ratio and collagen fibril thickness, where a thicker fibril gave a higher F/B ratio [63]. Intuitively one might expect thicker collagen fibrills to be more rigid, and thus stiffer, consistent with the results found here. However, the literatur differs. Seo et al. (2020) performed compression tests on collagen gels and found that gels with thicker collagen fibrils and larger pores are generally stiffer [64]. However, AFM measurements done by Wenger et al. (2007) on single collagen fibrils found no correlation between stiffness and collagen fibril thickness [65].

Another explanation for this apparent trend is collagen cross-linking. Collagen cross-linking has shown to increase tumor stiffness[13]. A study done by Bottòs et al. (2010) looked at the effect of collagen cross-linking on collagen organization in human cornea and saw that the group that had received collagen cross-linking treatment had a more organized collagen network compared to the control group [66]. The F/B ratio is related to collagen organization, as a higher F/B ratio is an indication of a more organized collagen network [39, 40, 67]. The collagen cross-linking could therefore increase the tumor stiffness at the same time as increasing F/B ratio. It is however important to note that the collagen organization in human corneas might differ from the collagen organization in tumors, and the relationship between collagen cross-linking and organization is therefore not a given fact. The trend seen here is, as mentioned, not statistically signifcant, but no other studies were found that looked at these two parameters. The relationship between F/B ratio and tumor stiffness could therefore be explored further.

Tumor mass

As can be seen in Figure 29 there seems to be a slight trend, especially for the Young's modulus, to decrease with increasing tumor mass. Chamming's et al. (2013) looked at the elasticity of a human tumor xenograft tumor model HBCx3 in vivo, using shear wave elastography as the tumors grew. The stiffness increased as the tumor grew, showing a strong correlation between size and stiffness ($r = 0.94$, $p < 0.0001$) [68]. However, there is one important difference between their study and this project. In this project, all tumors were implanted and excised at the same time, meaning that the difference between sizes is not related to the time the tumor has had to grow, as it is in the study by Chamming's et al. Another study, done by Nia et al. (2017) looked at the relationship between tumor size and stiffness in MMTV-M3C breast tumors, using an AFM. They found no correlation between tumor size and stiffness [69]. This might suggest that the negative trend seen here is only coincidental, which is supported by the fact that the correlation is not statistically significant.

5.6 Differences between center and periphery

As can be seen in Figure 22 and Figure 26, there is a slight tendency for all the experimental parameters to be higher in the periphery than center. Albeit not statistically significant, except for the control group regarding collagen area fraction, it is not unexpected. As explained in section 2.1.3, collagen can provide tissues with tensile strength, and the tensile forces are greater at the periphery. The collagen density is therefore higher in the tumor periphery than in the tumor center[1, 11]. Since there is a correlation between collagen area fraction and the Young's modulus, one could therefore also expect the Young's modulus to be higher in the tumor periphery. Collagen is more loosely packed in the center of the tumor [70]. The collagen fibers are also aligned perpendicularly with the tumor boundary at the periphery [70]. This is visible from the closeups of the tumor boundaries in Figure 23 and 24. More aligned collagen fibers would result in a higher F/B ratio at the tumor periphery.

5.7 Future work

In section 5.4 the effect of ultrasound and microbubbles on collagen and stiffness was discussed. However, the effect of collagen and stiffness on treatment success in terms of penetration length and nanoparticle accumulation has yet to be reviewed. As briefly mentioned in section 2.1.4, the dense extracellular matrix can hinder transport by acting as a physical barrier. An inverse relationship has been found between collagen content and diffusion distance of larger macromolecules [71]. While studies have shown that ultrasound and microbubbles fascilitate drug movement through the ECM, the extracellular matrix can still pose as a barrier [2]. A simulation done by Arango-Restrepo et al. (2021) found that the penetration length of nanoparticles in tumor interstitium was directly related to the tumor stiffness [72]. Again, it would be of interest to image the nanoparticle accumulation in the tumors. In addition to indicating positions of microbubble activation, it could also indicate areas of varying microbubble efficiency. By subsequently comparing this data to SHG tilescans, one can investigate if there is a trend between penetration distance and collagen content and organization. This could help increase the understanding of which tumor types might benefit more from ultrasound and microbubble treatment compared to others. Future work should also include more mice, as only five mice in each group is probably to small to detect any differences between control and treated. This is evident from the high heterogeneity found both between and within tumors in this thesis.

6 Conclusion

The first part of this project involved optimizing the curve fitting of Hertz model to force indentation curves acquired using the atomic force microscope. It was found that the best algorithm for determining the contact point was a combination of the goodness of fit, ΔE and ratio of variances algorithms, in accordance with was what found by Gavara (2016) [37]. The fit range was determined to be best when including the entire indentation depth, as this would also include all relevant information.

In the second part of this project, the effect of microbubbles and ultrasound on tumor stiffness and collagen density and organization was investigated. The effect on tumor stiffness was looked at using the atomic force microscope to measure the Young' modulus in control and treated 4T1 breast tumors, while the effect on collagen was investigated using second harmonic generation to look at collagen area fraction and F/B ratio. No statistical significant difference was found between the control and treated tumors for any of the parameters. However there is a clear positive correlation between Young's modulus and collagen area fraction, which is in accordance with literature. Future studies should aim to direct the AFM measurements by choosing the position of measurements in relation to perfused blood vessels and nanoparticle accumulation. Tilescans imaging perfused blood vessels and nanoparticles should also be superimposed with the SHG signal, to look at the variation in collagen based on the distance from perfused blood vessels were microbubbles have been active. By staining the nanoparticles used in combination with the ultrasound and microbubbles, one can also correlate differences in penetration length and accumulation with collagen content and orientation.

This was the first attempt at looking at the effect of microbubbles and ultrasound on the extracellular matrix in 4T1 tumors, and even though no results were found to make any conclusions on this effect, this project hopefully laid down some of the ground work for future research.

REFERENCES

[1] Triantafyllos Stylianopoulos, Lance L. Munn, and Rakesh K. Jain. Reengineering the physical microenvironment of tumors to improve drug delivery and efficacy: From mathematical modeling to bench to bedside. *Trends in Cancer*, 4, 2018.

[2] Sofie Snipstad, Krister Vikedal, Matilde Maardalen, Anna Kurbatskaya, Einar Sulheim, and Catharina de Lange Davies. Ultrasound and microbubbles to beat barriers in tumors: Improving delivery of nanomedicine. *Advanced Drug Delivery Reviews*, 177, 2021.

[3] Douglas Hanahan and Robert A. Weinberg. The hallmarks of cancer. *Cell*, 100, 2000.

[4] Sylvie Brassart-Pasco, Stéphane Brézillon, Bertrand Brassart, Laurent Ramont, Jean Baptiste Oudart, and Jean Claude Monboisse. Tumor microenvironment: Extracellular matrix alterations influence tumor progression. *Frontiers in Oncology*, 10, 2020.

[5] Jeff Hardin and Gregory Bertoni. *Becker's World of the cell*. Pearson Education Limited, 9 edition, 2018.

[6] Maria Kalli and Triantafyllos Stylianopoulos. Defining the role of solid stress and matrix stiffness in cancer cell proliferation and metastasis. *Frontiers in Oncology*, 8, 2018.

[7] Bruce Alberts, Alexander Johnson, Julian Lewis, Martin Raff, Keith Roberts, and Peter Walter. *The Extracellular Matrix of Animals*. Garland Science, 4th edition, 2002.

[8] Tongyan Liu, Chencheng Han, Siwei Wang, Panqi Fang, Zhifei Ma, Lin Xu, and Rong Yin. Cancer-associated fibroblasts: An emerging target of anti-cancer immunotherapy. *Journal of Hematology and Oncology*, 12, 2019.

[9] Raghu Kalluri. The biology and function of fibroblasts in cancer. *Nature Reviews Cancer*, 16, 2016.

[10] Raghu Kalluri and Michael Zeisberg. Fibroblasts in cancer. *Nature Reviews Cancer*, 6:392–401, 5 2006.

[11] Jiacheng Huang, Lele Zhang, Dalong Wan, Lin Zhou, Shusen Zheng, Shengzhang Lin, and Yiting Qiao. Extracellular matrix and its therapeutic potential for cancer treatment. *Signal Transduction and Targeted Therapy*, 6, 2021.

[12] Soo Hyun Kim, Jeremy Turnbull, and Scott Guimond. Extracellular matrix and cell signalling: The dynamic cooperation of integrin, proteoglycan and growth factor receptor. *Journal of Endocrinology*, 209, 2011.

[13] Kandice R. Levental, Hongmei Yu, Laura Kass, Johnathon N. Lakins, Mikala Egeblad, Janine T. Erler, Sheri F.T. Fong, Katalin Csiszar, Amato Giaccia, Wolfgang Weninger, Mitsuo Yamauchi, David L. Gasser, and Valerie M. Weaver. Matrix crosslinking forces tumor progression by enhancing integrin signaling. *Cell*, 139, 2009.

[14] Arun K. Iyer, Greish Khaled, Jun Fang, and Hiroshi Maeda. Exploiting the enhanced permeability and retention effect for tumor targeting. *Drug Discovery Today*, 11, 2006.

[15] Atin Saha and Mahan Mathur. Ultrasound physics overview. In Jinlei Li, Robert Ming-Der Chow, Nalini Vadivelu, and Alan David Kaye, editors, *Ultrasound Fundamentals*, pages 3–16. Springer International Publishing, 2021.

[16] Susannah J. Patey and James P. Corcoran. Physics of ultrasound. *Anaesthesia and Intensive Care Medicine*, 22, 2021.

[17] Alexander EJ Powles, David J. Martin, Irving TP Wells, and Christopher R. Goodwin. Physics of ultrasound. *Anaesthesia and Intensive Care Medicine*, 19, 2018.

[18] Vincent Chan and Anahi Perlas. Basics of ultrasound imaging. In Samer N. Narouze, editor, *Atlas of Ultrasound-Guided Procedures in Interventional Pain Management*. Springer, 2011.

[19] Sayan Mullick Chowdhury, Lotfi Abou-Elkacem, Taehwa Lee, Jeremy Dahl, and Amelie M. Lutz. Ultrasound and microbubble mediated therapeutic delivery: Underlying mechanisms and future outlook. *Journal of Controlled Release*, 326, 2020.

[20] M. Mischi, N.G. Rognin, and M.A. Averkiou. Ultrasound imaging modalities. *Comprehensive Biomedical Physics*, pages 361–385, 1 2014.

[21] Mario L. Fabiilli, Kevin J. Haworth, Nasir H. Fakhri, Oliver D. Kripfgans, Paul L. Carson, and J. Brian Fowlkes. The role of inertial cavitation in acoustic droplet vaporization. *IEEE Transactions on Ultrasonics, Ferroelectrics, and Frequency Control*, 56, 2009.

[22] Hao Li Liu, Ching Hsiang Fan, Chien Yu Ting, and Chih Kuang Yeh. Combining microbubbles and ultrasound for drug delivery to brain tumors: Current progress and overview. *Theranostics*, 4, 2014.

[23] Franz J. Giessibl. Advances in atomic force microscopy. *Reviews of Modern Physics*, 75, 2003.

[24] Ben Rogers, Jesse Adams, and Sumita Pennathur. *Nanotechnology: Understanding small systems*. Taylor and Francis Group, Florida, 3 edition, 2015.

[25] R. Lal and S. A. John. Biological applications of atomic force microscopy. *American Journal of Physiology - Cell Physiology*, 266, 1994.

[26] Jeffrey L. Hutter and John Bechhoefer. Calibration of atomic-force microscope tips. *Review of Scientific Instruments*, 64, 1993.

[27] Engineering ToolBox. Stress, strain and young's modulus. https://www.engineeringtoolbox.com/stress-strain-d_950.html, 2005. Accessed 2 March 2022.

[28] Ankur Vaidya and Kamla Pathak. 17 - mechanical stability of dental materials. In Abdullah M. Asiri, Inamuddin, and Ali Mohammad, editors, *Applications of Nanocomposite Materials in Dentistry*, Woodhead Publishing Series in Biomaterials, pages 285–305. Woodhead Publishing, 2019.

[29] M. Benabdi and A.A. Roche. Mechanical properties of thin and thick coatings applied to various substrates. part ii. young's modulus determination of coating materials. *Journal of Adhesion Science and Technology*, 11(3):373–391, 1997.

[30] H. Hertz. Über die berührung fester elastischer körper und Über die härte. *Journal fur die reine und angewandte Mathematik*, 92:156–171, 1881.

[31] Emilios K. Dimitriadis, Ferenc Horkay, Julia Maresca, Bechara Kachar, and

Richard S. Chadwick. Determination of elastic moduli of thin layers of soft material using the atomic force microscope. *Biophysical Journal*, 82(5):2798–2810, 2002.

[32] Jon Jincai Zhang. Chapter 2 - rock physical and mechanical properties. In Jon Jincai Zhang, editor, *Applied Petroleum Geomechanics*, pages 29–83. Gulf Professional Publishing, 2019.

[33] Tanya Glozman and Haim Azhari. A method for characterization of tissue elastic properties combining ultrasonic computed tomography with elastography. *Journal of Ultrasound in Medicine*, 29(3):387–398, 2010.

[34] S. V. Kontomaris and A. Malamou. Hertz model or oliver pharr analysis? tutorial regarding afm nanoindentation experiments on biological samples. *Materials Research Express*, 7, 2020.

[35] Yuri M. Efremov, Wen Horng Wang, Shana D. Hardy, Robert L. Geahlen, and Arvind Raman. Measuring nanoscale viscoelastic parameters of cells directly from afm force-displacement curves. *Scientific Reports*, 7, 2017.

[36] Andrés Rubiano, Carly Galitz, and Chelsey S. Simmons. Mechanical characterization by mesoscale indentation: Advantages and pitfalls for tissue and scaffolds. *Tissue Engineering - Part C: Methods*, 25, 2019.

[37] Núria Gavara. Combined strategies for optimal detection of the contact point in afm force-indentation curves obtained on thin samples and adherent cells. *Scientific Reports*, 6, 2016.

[38] Robert W. Boyd. *Nonlinear Optics*, chapter The Nonlinear Optical Susceptibility, pages 1–67. Academic Press, Burlington, 3rd edition, 2008.

[39] Xiyi Chen, Oleg Nadiarynkh, Sergey Plotnikov, and Paul J. Campagnola. Second harmonic generation microscopy for quantitative analysis of collagen fibrillar structure. *Nature Protocols*, 7, 2012.

[40] Rebecca M. Williams, Warren R. Zipfel, and Watt W. Webb. Interpreting second-harmonic generation images of collagen i fibrils. *Biophysical Journal*, 88, 2005.

[41] Ingvil Bjørnæs and Einar K. Rofstad. Microvascular permeability to macromolecules in human melanoma xenografts assessed by contrast-enhanced mri - intertumor and intratumor heterogeneity. *Magnetic Resonance Imaging*, 19, 2001.

[42] *Central Limit Theorem*, pages 66–68. Springer New York, New York, NY, 2008.

[43] W.S. Rasband. Imagej, U. S. National Institutes of Health, Bethesda, Maryland, USA. https://imagej.nih.gov/ij/, 1997-2018.

[44] Shalini V. Rao, Kurt I. Draget, and Catherine Taylor Nordgård. Young's modulus of tumour tissue from an in vivo breast cancer model- effect of treatment with guluronate oligosaccharides. *Annual Transactions of the Nordic Rheology Society*, 27:41–45, 2019.

[45] Johannes Riegler, Yassin Labyed, Stephen Rosenzweig, Vincent Javinal, Alessandra Castiglioni, Claudia X. Dominguez, Jason E. Long, Qingling Li, Wendy Sandoval, Melissa R. Junttila, Shannon J. Turley, Jill Schartner, and Richard A.D. Carano. Tumor elastography and its association with collagen and the tumor microenvironment. *Clinical Cancer Research*, 24, 2018.

[46] Chrysovalantis Voutouri, Myrofora Panagi, Fotios Mpekris, Andreas Stylianou,

Christina Michael, Michalakis A. Averkiou, John D. Martin, and Triantafyllos Stylianopoulos. Endothelin inhibition potentiates cancer immunotherapy revealing mechanical biomarkers predictive of response. *Advanced Therapeutics*, 4, 2021.

[47] Nafiseh Poornejad, Timothy S. Frost, Daniel R. Scott, Brinden B. Elton, Paul R. Reynolds, Beverly L. Roeder, and Alonzo D. Cook. Freezing/thawing without cryoprotectant damages native but not decellularized porcine renal tissue. *Organogenesis*, 11, 2015.

[48] Xin Xu, Zhiyu Li, Luyao Cai, Sarah Calve, and Corey P. Neu. Mapping the nonreciprocal micromechanics of individual cells and the surrounding matrix within living tissues. *Scientific Reports*, 6, 2016.

[49] Delphine Sicard, Laura E. Fredenburgh, and Daniel J. Tschumperlin. Measured pulmonary arterial tissue stiffness is highly sensitive to afm indenter dimensions. *Journal of the Mechanical Behavior of Biomedical Materials*, 74, 2017.

[50] Xiaoxing Han, Ryan M. Burke, Martha L. Zettel, Ping Tang, and Edward B. Brown. Second harmonic properties of tumor collagen: determining the structural relationship between reactive stroma and healthy stroma. *Optics Express*, 16, 2008.

[51] Christiana Polydorou, Fotios Mpekris, Panagiotis Papageorgis, Chrysovalantis Voutouri, and Triantafyllos Stylianopoulos. Pirfenidone normalizes the tumor microenvironment to improve chemotherapy. *Oncotarget*, 8, 2017.

[52] Einar Sulheim, Jana Kim, Annemieke van Wamel, Eugene Kim, Sofie Snipstad, Igor Vidic, Ingeborg Hovde Grimstad, Marius Widerøe, Sverre H. Torp, Steinar Lundgren, David J. Waxman, and Catharina de Lange Davies. Multi-modal characterization of vasculature and nanoparticle accumulation in five tumor xenograft models. *Journal of Controlled Release*, 279, 2018.

[53] Gulisa Turashvili and Edi Brogi. Tumor heterogeneity in breast cancer. *Frontiers in Medicine*, 4, 2017.

[54] Santiago Ramón y Cajal, Marta Sesé, Claudia Capdevila, Trond Aasen, Leticia De Mattos-Arruda, Salvador J. Diaz-Cano, Javier Hernández-Losa, and Josep Castellví. Clinical implications of intratumor heterogeneity: challenges and opportunities. *Journal of Molecular Medicine*, 98, 2020.

[55] T. Ushiki. The three-dimensional ultrastructure of the collagen fibers, reticular fibers and elastic fibers: a review. *Kaibogaku zasshi. Journal of anatomy*, 67, 1992.

[56] Si Jie Hao, Yuan Wan, Yi Qiu Xia, Xin Zou, and Si Yang Zheng. Size-based separation methods of circulating tumor cells. *Advanced Drug Delivery Reviews*, 125, 2018.

[57] Einar Sulheim, Ingunn Hanson, Sofie Snipstad, Krister Vikedal, Yrr Mørch, Yves Boucher, and Catharina de Lange Davies. Sonopermeation with nanoparticle-stabilized microbubbles reduces solid stress and improves nanomedicine delivery to tumors. *Advanced Therapeutics*, 4, 2021.

[58] Qianyun Zhang, Hai Jin, Liping Chen, Qiaoli Chen, Yan He, Yuwen Yang, Suihong Ma, Shuyi Xiao, Fen Xi, Qiong Luo, and Jianhua Liu. Effect of ultrasound combined with microbubble therapy on interstitial fluid pressure

and vx2 tumor structure in rabbit. *Frontiers in Pharmacology*, 10, 2019.

[59] Tong Li, Yak Nam Wang, Tatiana D. Khokhlova, Samantha D'Andrea, Frank Starr, Hong Chen, Jeannine S. McCune, Linda J. Risler, Afshin Mashadi-Hossein, and Joo Ha Hwang. Pulsed high-intensity focused ultrasound enhances delivery of doxorubicin in a preclinical model of pancreatic cancer. *Cancer Research*, 75, 2015.

[60] Sangmin Lee, Hyounkoo Han, Heebeom Koo, Jin Hee Na, Hong Yeol Yoon, Kyung Eun Lee, Hyukjin Lee, Hyuncheol Kim, Ick Chan Kwon, and Kwangmeyung Kim. Extracellular matrix remodeling in vivo for enhancing tumor-targeting efficiency of nanoparticle drug carriers using the pulsed high intensity focused ultrasound. *Journal of Controlled Release*, 263, 2017.

[61] Lena Wullkopf, Ann Katrine V. West, Natascha Leijnse, Thomas R. Cox, Chris D. Madsen, Lene B. Oddershede, and Janine T. Erler. Cancer cells' ability to mechanically adjust to extracellular matrix stiffness correlates with their invasive potential. *Molecular Biology of the Cell*, 29, 2018.

[62] Kathleen Burke and Edward Brown. The use of second harmonic generation to image the extracellular matrix during tumor progression. *IntraVital*, 3, 2014.

[63] Shi-Wei Chu, Shih-Peng Tai, Ming-Che Chan, Chi-Kuang Sun, I-Ching Hsiao, Chi-Hung Lin, Yung-Chih Chen, and Bai-Ling Lin. Thickness dependence of optical second harmonic generation in collagen fibrils. *Optics Express*, 15, 2007.

[64] Bo Ri Seo, Xingyu Chen, Lu Ling, Young Hye Song, Adrian A. Shimpi, Siyoung Choi, Jacqueline Gonzalez, Jiranuwat Sapudom, Karin Wang, Roberto Carlos Andresen Eguiluz, Delphine Gourdon, Vivek B. Shenoy, and Claudia Fischbach. Collagen microarchitecture mechanically controls myofibroblast differentiation. *Proceedings of the National Academy of Sciences of the United States of America*, 117, 2020.

[65] Marco P.E. Wenger, Laurent Bozec, Michael A. Horton, and Patrick Mesquidaz. Mechanical properties of collagen fibrils. *Biophysical Journal*, 93, 2007.

[66] Kátia Mantovani Bottós, Ana Luisa Hofling-Lima, Manuela C. Barbosa, Jose Bonifacio Barbosa, Juliana L. Dreyfuss, Paulo Schor, and Helena B. Nader. Effect of collagen cross-linking in stromal fibril organization in edematous human corneas. *Cornea*, 29, 2010.

[67] Gavin Tjin, Paul Xu, Scott H. Kable, Eleanor P. W. Kable, and Janette K. Burgess. Quantification of collagen i in airway tissues using second harmonic generation. *Journal of Biomedical Optics*, 19, 2014.

[68] Foucauld Chamming'S, H. Latorre-Ossa, M. A. Le Frère-Belda, V. Fitoussi, T. Quibel, F. Assayag, E. Marangoni, G. Autret, D. Balvay, L. Pidial, J. L. Gennisson, M. Tanter, C. A. Cuenod, O. Clément, and L. S. Fournier. Shear wave elastography of tumour growth in a human breast cancer model with pathological correlation. *European Radiology*, 23, 2013.

[69] Hadi T. Nia, Hao Liu, Giorgio Seano, Meenal Datta, Dennis Jones, Nuh Rahbari, Joao Incio, Vikash P. Chauhan, Keehoon Jung, John D. Martin, Vasileios Askoxylakis, Timothy P. Padera, Dai Fukumura, Yves Boucher, Francis J. Hornicek, Alan J. Grodzinsky, James W. Baish, Lance L. Munn, and Rakesh K. Jain. Solid

stress and elastic energy as measures of tumour mechanopathology. *Nature Biomedical Engineering*, 1, 2017.

[70] Kristin M. Riching, Benjamin L. Cox, Max R. Salick, Carolyn Pehlke, Andrew S. Riching, Susan M. Ponik, Benjamin R. Bass, Wendy C. Crone, Yi Jiang, Alissa M. Weaver, Kevin W. Eliceiri, and Patricia J. Keely. 3d collagen alignment limits protrusions to enhance breast cancer cell persistence. *Biophysical Journal*, 107, 2015.

[71] Paolo A. Netti, David A. Berk, Melody A. Swartz, Alan J. Grodzinsky, and Rakesh K. Jain. Role of extracellular matrix assembly in interstitial transport in solid tumors. *Cancer Research*, 60, 2000.

[72] Andrés Arango-Restrepo, J. Miguel Rubi, Signe Kjelstrup, Bjørn Atle J. Angelsen, and Catharina de Lange Davies. Enhancing carrier flux for efficient drug delivery in cancer tissues. *Biophysical Journal*, 120:5255–5266, 12 2021.

APPENDIX A
PYTHON SCRIPT FOR ANALYZING AFM FORCE CURVES

Underneath is the python script for curve fitting Hertz model to AFM force curves. The script takes in data from one section and assumes a total of 90 force curves in this section, and 10 force curves per position. The script also assumes a tip diameter of 25 µm, and a biological sample with Poisson ratio 0.5.

```
# Importing packages
import numpy as np
import matplotlib.pyplot as plt
import math
from scipy.optimize import curve_fit
import scipy as sp
import csv
import os

def txt_file_reader(filename):
    with open("{}".format(filename)) as file:
        csv_reader = csv.reader(file, delimiter = "\t")
        force = []
        distance = []
        deflection = []
        linecount=0
        for row in csv_reader:
            if linecount == 0:
                linecount+=1
            else:
                try:
                    force.append(float(row[4].replace(',', '.'))*0.001)
                    distance.append(float(row[0].replace(',', '.'))*0.001)
                    deflection.append(float(row[2].replace(',', '.'))
   *0.001)
                except:
                    pass

    for i in range(1,len(force)):
        force[i] = force[i] - force[0]
        deflection[i] = deflection[i] - deflection[0]
    force[0] = 0
    deflection[0] = 0
    return force,distance, deflection

def find_nearest(array,value):
            idx = np.searchsorted(array, value, side="left")
            if idx > 0 and (idx == len(array) or math.fabs(value - array[
   idx-1]) < math.fabs(value - array[idx])):
                return idx-1
            else:
                return idx

def hertz_law(d,E,k):
    F=4/3*E/(1-0.5**2)*np.sqrt(12.5)*d**(3/2)+k
```

```
    return F

model = np.vectorize(hertz_law)

def r_squared(y,function):
            y_bar=np.mean(y)
            ss_res=np.sum((y-function)**2)
            ss_tot=np.sum((y-y_bar)**2)
            return 1 - ss_res/ss_tot

# Initial set up

kpa_values = []
r_squared_values = []
tumor_type = "NAME_OF_SECTION"
numbers=["{0:03}".format(i) for i in range(90)]
directory = "PATH_TO_FILE"
save_directory_png = "SAVE_PATH_FOR_IMAGES"

# Main loop

for i in numbers:
    # Importing file
    name = "{}.{}".format(tumor_type,i)
    fname="{}{}.txt".format(directory,name)

    file_exist = os.path.exists(fname)
    if file_exist == True:
        force, distance, deflection = txt_file_reader(fname)
        distance = [i-j for i,j in zip(distance,deflection)]

        ## Determining contact point

        # Goodness of fit and delta E
        r = [0,0,0,0,0]
        E = [0,0,0,0,0]
        for i in range(5,find_nearest(force,0.5)):
            force_fit,distance_fit = [],[]

            try:
                stopindex = find_nearest(distance,distance[i]+0.1)
            except:
                stopindex = len(distance)-1

            value = distance[i]

            distance_fit = [j-value for j in distance]

            force_fit = force[i:stopindex+1]
            distance_fit = distance_fit[i:stopindex+1]
```

```
            param, param_cov = curve_fit(hertz_law, distance_fit, force_fit
)

            E.append(param[0])
            r.append(r_squared(force_fit,model(distance_fit,param[0],param
[1])))

        cp_gof = r.index(max(r))

        dE=[0,0,0]
        logE = np.log(E)
        for i in range(3,len(logE)-3):
            dlogE = -1/60*logE[i-3]+3/20*logE[i-2]-3/4*logE[i-1]+3/4*logE[i
+1]-3/20*logE[i+2]+1/60*logE[i+3]
            dE.append(-dlogE)

        dE = np.nan_to_num(dE, neginf = 0.0)
        dE = dE.tolist()

        cp_dE = dE.index(max(dE))

        # Ratio of variances

        rov=[0]*50

        for i in range(50,find_nearest(force,0.5)):
            rvar = np.var(deflection[i+1:i+50])/np.var(deflection[i-50:i
-1])
            rov.append(rvar)

        cp_rov = rov.index(max(rov))

        # Combined strategies

        combined = [a*b*c for a,b,c in zip(r,rov,dE)]
        cp = combined.index(max(combined))

        # Converting distance to indentation depth

        value = distance[cp]
        distance = [j-value for j in distance]

        # Determining fit interval

        stopindex = len(distance)

        force_fit = []
        distance_fit = []

        force_fit = force[cp:stopindex+1]
        distance_fit = distance[cp:stopindex+1]
```

```
        # Performing curve fit
        param,param_cov=curve_fit(hertz_law,distance_fit,force_fit)

        r_squared_value=r_squared(force_fit,model(distance_fit,param[0],
    param[1]))


        # Plotting curve and saving figure
        fig, ax = plt.subplots(figsize=(10,6))
        ax.plot(distance,force,"-.",label="Data")
        ax.plot(distance_fit,model(distance_fit, param[0],param[1]),label="
    Hertz model")
        plt.title(name,weight="bold")
        plt.xlabel("Indentation (\u03bcm)")
        plt.ylabel("Force (nN)")
        ax.text(0.2,0.91,'E=%2f \nr\u00b2=%2f'%(param[0],r_squared_value),
    bbox=dict(facecolor='orange', alpha=0.1), transform=ax.transAxes)
        ax.legend()
        plt.savefig("{}{}.png".format(save_directory_png,name))
        plt.close()

        # Adding Young's modulus and r_squared to main lists:
        kpa_values.append(param[0])
        r_squared_values.append(r_squared_value)

    else:
        kpa_values.append("False")

# Sorting values into positions

positions = [["Position {}".format(i)] for i in range(1,10)]

for i in range(0,9):
    for j in range(i*10,i*10+10):
        positions[i].append(kpa_values[j])

for i in positions:
    k = 0
    while k<len(i):
        if i[k] == "False":
            i.remove(i[k])
        else:
            k +=1


# Finding average Young's modulus per position

pos_avg = [["Position {}".format(i)] for i in range(1,10)]


count = 0
for i in positions:
```

```
    sum1 = 0
    for j in range(1,len(i)):
        sum1 += i[j]

    try:
        avg_list = sum1/(len(i)-1)
    except:
        avg_list = "NA"
    pos_avg[count].append(avg_list)
    pos_avg[count].append("N={}".format(len(i)-1))
    count += 1

# Saving data
def save_data(data,rdata,mdata,pdata):
    f= open('{}Youngsmodulus-{}.txt'.format(directory,tumor_type), 'w')
    for i in data:
        f.write(str(i))
        f.write("\n")
    f.close()
    f= open('{}Meandata-{}.txt'.format(directory,tumor_type), 'w')
    for i in mdata:
        f.write(str(i))
        f.write("\n")
    f.close()
    f= open('{}Posdata-{}.txt'.format(directory,tumor_type), 'w')
    for i in pdata:
        for j in i:
            f.write(str(j))
            f.write("\n")
    f.close()
    f= open('{}R_values-{}.txt'.format(directory,tumor_type), 'w')
    for i in rdata:
        f.write(str(i))
        f.write("\n")
    f.close()

save_data(kpa_values,r_squared_values,pos_avg,positions)
```

APPENDIX B
CORRELATING AFM MEASUREMENTS WITH SHG IMAGES

A trial was made in correlating the AFM measurements with SHG tilescans. The measurements were first done using the AFM. Prior to the measurements, it was ensured that the AFM probe was positioned in the middle of the screen, using the knobs on the microscope. For each position, the coordinates were written down, and a brightfield image was taken, using the Andor iXon DU 897_BV EMCCD camera connected to the Axio Observer Z1. The same was done for the maximum and minimum x and y coordinates. A coordinate system was made in Microsoft Excel, an example of which is shown in Figure 30.

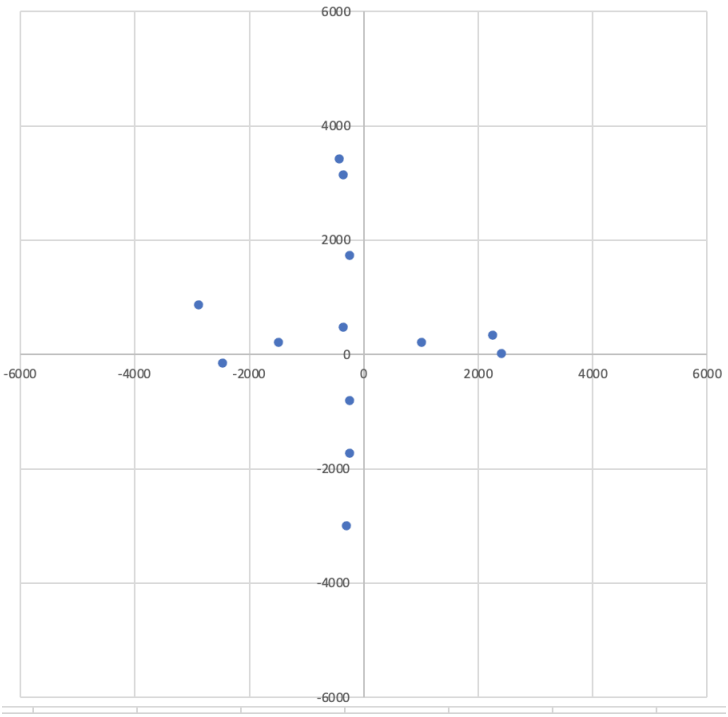

Figure 30: Coordinate system of positions measured with the AFM.

After measurements, the D-PBS was dried off the object glass. A droplet of Vectashield was put on top, followed by a coverglass. Tilescans were then taken using the Leica SP8, in both the forward and backward direction, the details of which are explained in section 3.3.2. One detail that was omitted when doing this analysis, was the process of adjusting for Köhler illumination. This wasn't done for any of the thirty sections measured with both AFM and SHG, which resulted in an improper condenser position, and a low forward SHG signal.

For the correlation of the tilescans with the AFM measurements, the backward image was used, as this had the strongest signal. The brightness was adjusted to max, to get a good visualization of the tumor edges. An example of this is shown in Figure 31.

The acquired coordinate system in Figure 30 was then superimposed on the backwards tilescan image, and scaled according to the scalebar. The image was then

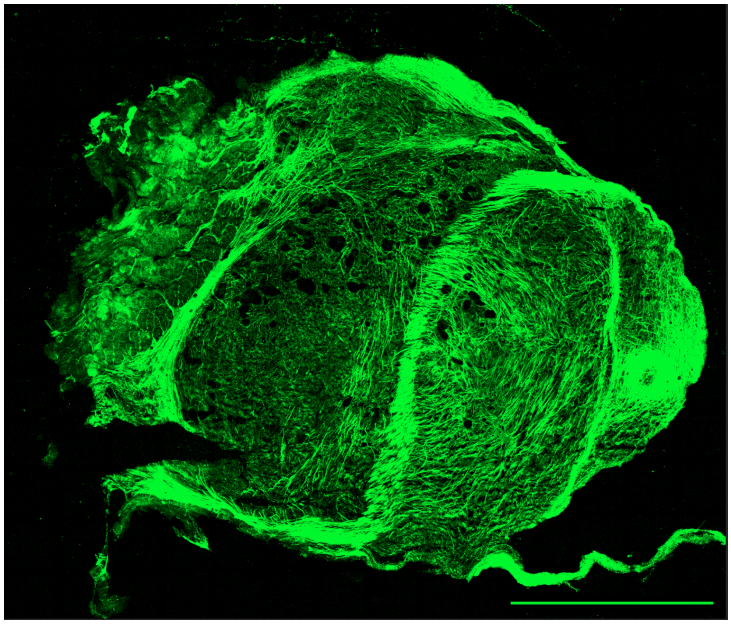

Figure 31: Image obtained from the backward SHG signal, after the brightness have been adjusted to maximum.

rotated and/or flipped, to get a good correlation between the tumor edges and the maximum and minimum x and y coordinates. This is illustrated in Figure 32 The placement of the object glass on the AFM and the Leica SP8 wasn't always consistent, so the amount of rotation, and whether the image needed a horizontal or vertical flip needed to be evaluated for each image. The superimposition was done in Adobe Photoshop CC 2019.

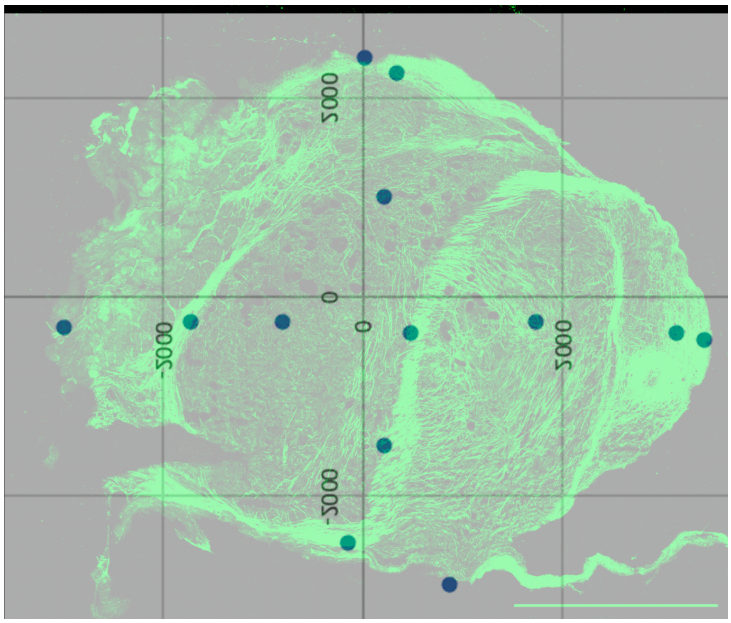

Figure 32: The coordinate system in Figure 30 superimposed on the tilescan in Figure 31. The coordinate system has been scaled and rotated to match the edges of the tumor.

The brightfield images acquired by the AFM at the tumor edges (maximum and minimum x and y) were then also superimposed on the tilescan according to the coordinate system. First, ImageJ[43] was used to obtain the size of the AFM image, which was done using the "Set scale" option and using the knowledge that the AFM probe is 25 µm in diameter. Again, the images were scaled according to the scalebar of the tilescan, and rotated and/or flipped. The images were superimposed on the coordinate system and tilescan, with the middle of each image corresponding to each coordinate. This was done to verify the position of the coordinates, as certain features of the AFM images were present in the SHG image, especially at the tumor edges. The result of this is shown in Figure 33.

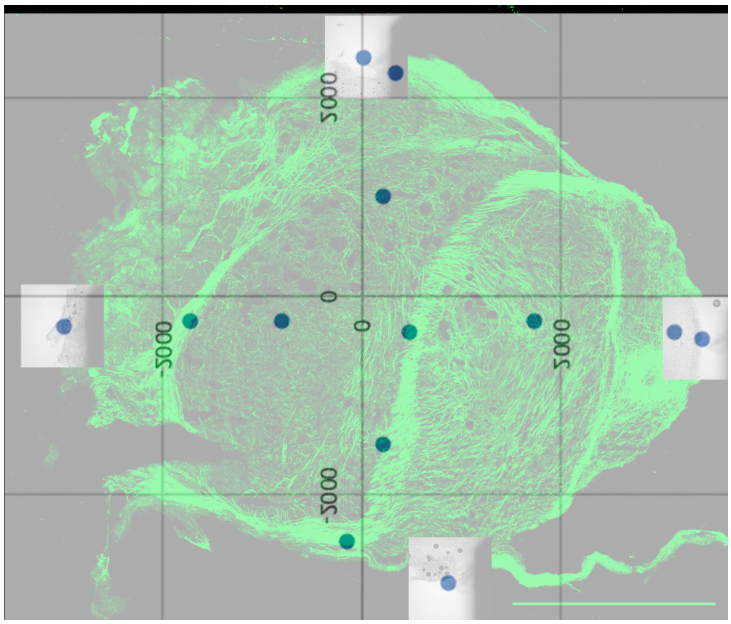

Figure 33: The brightfield images obtained with the AFM, positioned with the center at their respective coordinate.

As can be seen in the figure, some of the brightfield image features does not match with the corresponding features in the SHG image (the edges on the right do not line up). The brightfield images were moved to their correct position. Then, the coordinate system was shifted to try and match the coordinates with their respective brightfield images. Most of the time, it was not possible to find a rotation that lead to matching of all the coordinates with their respective brightfield images, and the coordinate system was then shifted in a way were all the coordinates were within their respective images as close to the center as possible. This is illustrated in Figure 34.

The remaining brightfield images, of the measured positions, were then moved to their respective coordinates. The images were compared to the SHG tilescan underneath, and the AFM image was moved slightly if certain features were recognizable and not matching.The entire brightfield image was then overlayed with a white color, and the image was imported into ImageJ. The white squares were then selected using the magic wand tool, and defined the ROIs in the image. The edges of the tumor was then selected, according to section subsubsection 3.4.1, and the outside of the tumor

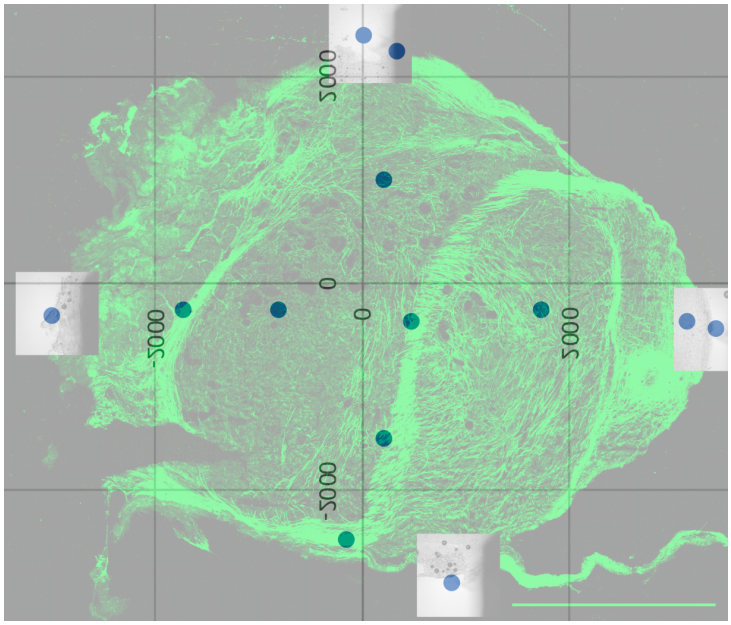

Figure 34: The same image as in Figure 33 after the brightfield images have been moved to their correct positions, and the coordinate system has been shifted to match.

was subtracted from the ROIs at the tumor edge. The resulting ROIs are highlighted in Figure 35

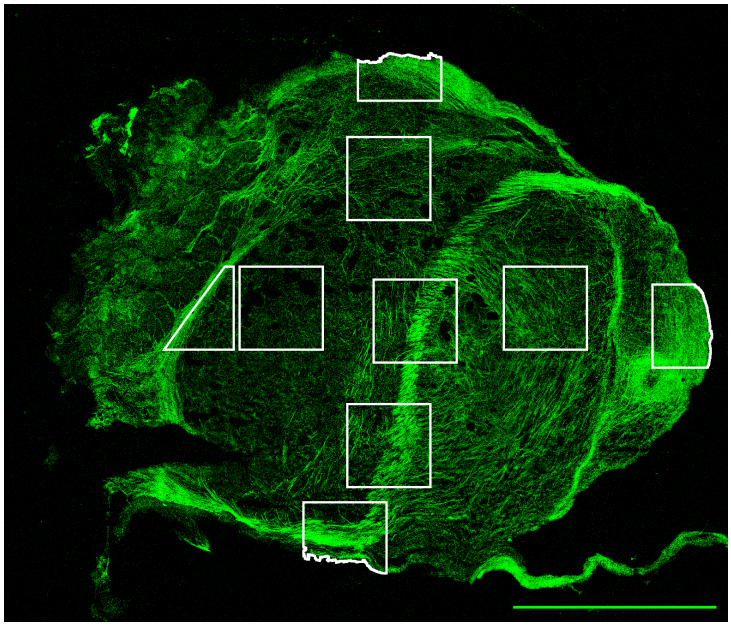

Figure 35: The region of interests obtained after superimposition of the AFM images on the SHG tilescan, and the areas outside of the tumor has been removed.

The F/B ratio and collagen density was then measured at each ROI, using the raw tumor images. The measurements were then correlated with the Young's modulus of the position at each ROI. The result of this correlation done for thirty tumor sections is shown in Figure 36, where each data point represents one ROI, or position.

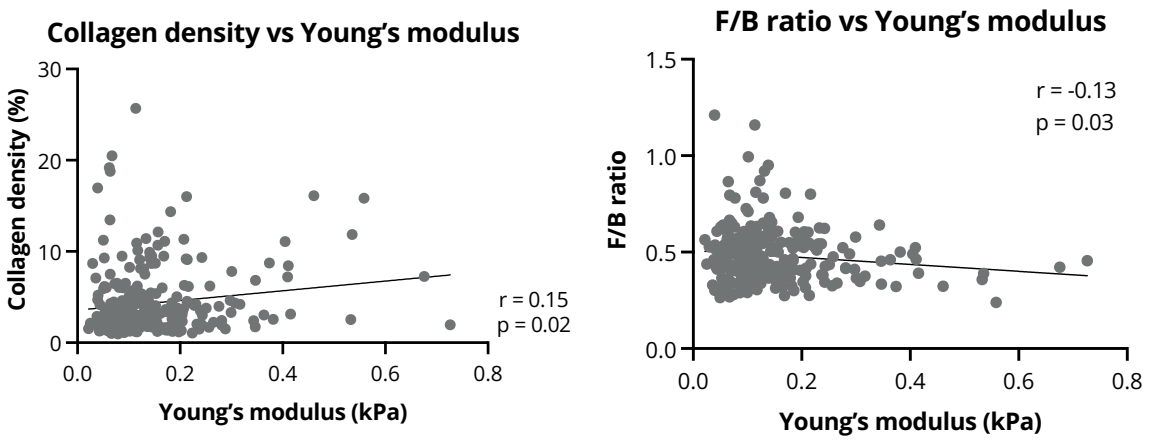

(a) (b)

Figure 36: The correlation between the measured values at the ROIs, illustrated for one tumor in Figure 35, with the Young's modulus found at that position.

A very weak correlation was found for the comparisons, both being statistically significant. As the microscope wasn't adjusted for Köhler between each measurement, there is a lot of uncertainty regarding the signal in the SHG photos. The forward SHG signal, and thus both the calculated F/B ratio and collagen density, is very dependent on the height of the condenser lens. If the height had been adjusted between measurements, it would definitely affect the result. These SHG images were therefore not included in the main report. It should be noted that there is also a lot of uncertainty related to the positioning of the coordinates and the brightfield images. The ROIs were therefore kept quite large, to make sure that they encompassed the measured position. The brightfield images are approximately 800 by 800 μm, while each position is only 25 by 25 μm. Given the large heterogeneity in the tissue, a strong correlation between the measured ROIs and the positions would therefore be unlikely in this case.

APPENDIX C
PYTHON SCRIPT FOR CALCULATING INTER- AND INTRAHETEROGENEITY

Underneath is the python script for calculating inter- and intraheterogeneity of a sample population divided into subgroups. In this script it is assumed that all the data in one column belong to the same subgroup.

```
# Importing packages
import numpy as np
import math
import csv

def txt_file_reader(fileN,fileD):
    with open("{}{}".format(fileD,fileN)) as file:
        csv_reader = csv.reader(file, delimiter = "\t")
        subgroups = [[] for i in range (0,10)]
        samples = []
        linecount=0
        for row in csv_reader:
            if linecount <2:
                linecount+=1
            else:
                for i in range(len(row)):
                    subgroups[i].append(float(row[i]))
                    samples.append(float(row[i]))
    return subgroups, samples

filename = "FILENAME"
directory = "PATH_TO_FILE"

subgroups,samples = txt_file_reader(filename,directory)

variances = []
n_1 = []
for i in subgroups:
    variances.append(np.var(i))
    n_1.append(len(i)-1)

var_intra_sum = 0
total_n = 0

for i in range(len(variances)):
    var_intra_sum += variances[i]*n_1[i]
    total_n += len(subgroups[i])

var_intra = var_intra_sum/(total_n-len(subgroups))


var_inter = np.var(samples)
f = var_intra/(var_intra+var_inter)

info = [var_intra,var_inter,f]
```

```
#Save data
with open('{}SAVE_FILENAME.csv'.format(directory), 'a') as f:
    f.write(str(info))
    f.write("\n")
```

APPENDIX D
EXAMPLES OF CONTACT POINT ALGORITHMS ON AFM FORCE CURVES

Figure 37 shows examples of force curves fitted with different contact point algorithms, that differ from the force curve used as an example in section 4.1. Figure 37(a) shows an example of a curve where the fit is relatively bad (low r^2 value) for all algorithms. (b) Shows an example of a curve that doesn't follow the standard trend explained in section 4.1 where the ΔE algorithm underestimates the contact point, here it is clearly overestimating. (c) Shows an example of a force curve where determining the contact point might be hard, and where the combined strategies algorithm fail. In this case, if the contact point was to be chosen manually it would have been somewhere between the combined strategies and ΔE contact point.

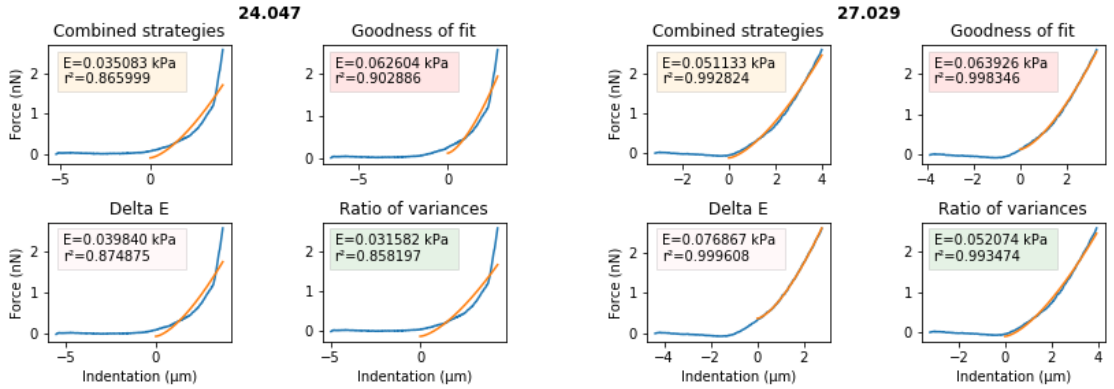

(a)

(b)

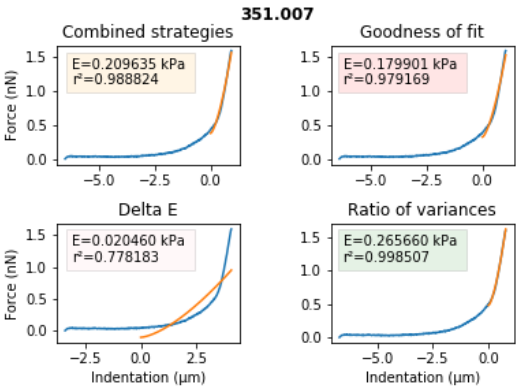

(c)

Figure 37: Figure showing three different force curves obtained using the AFM. The three force curves have been fitted with four different contact point algorithms and shows examples of three different situations.

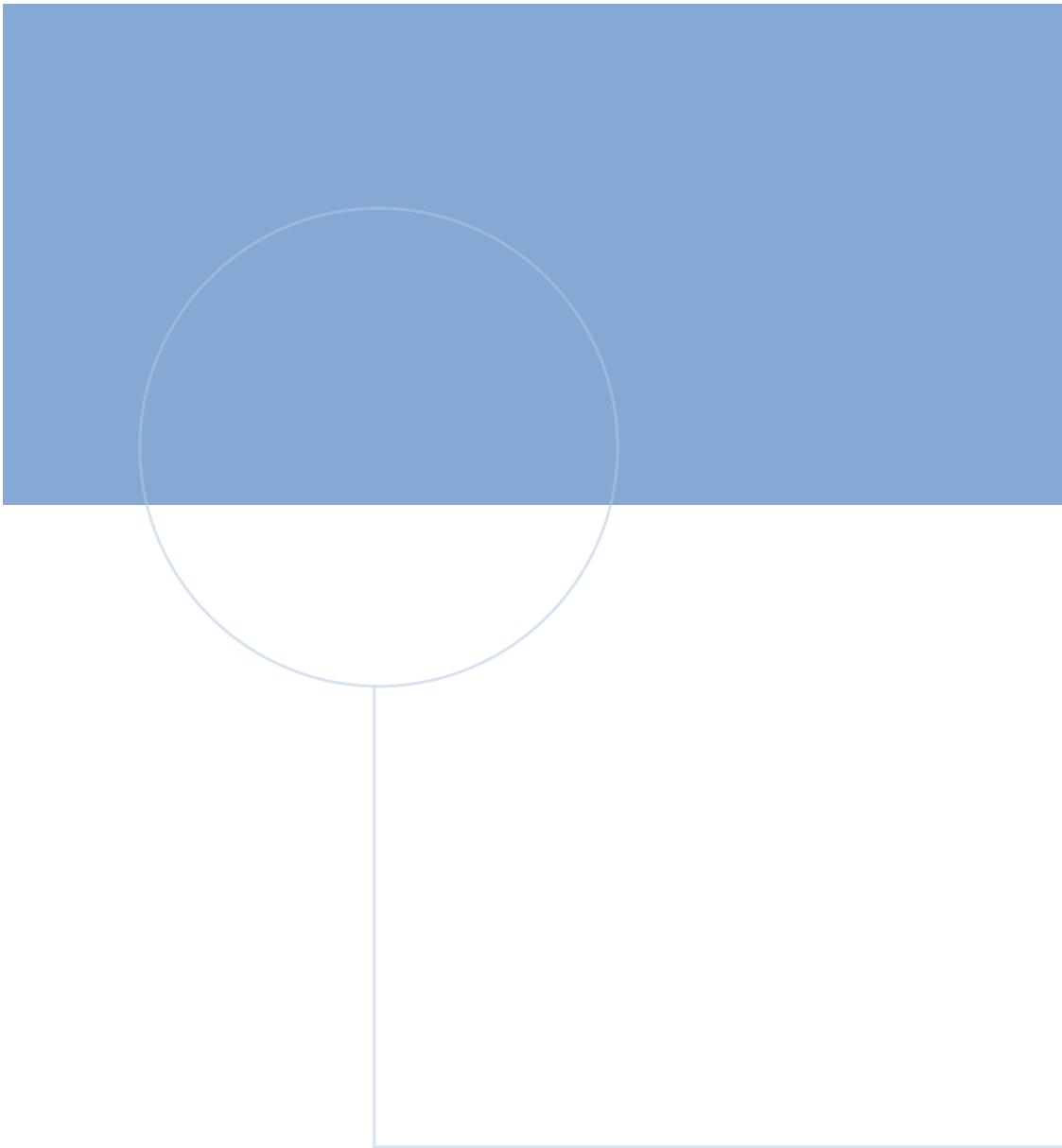

NTNU

Kunnskap for en bedre verden